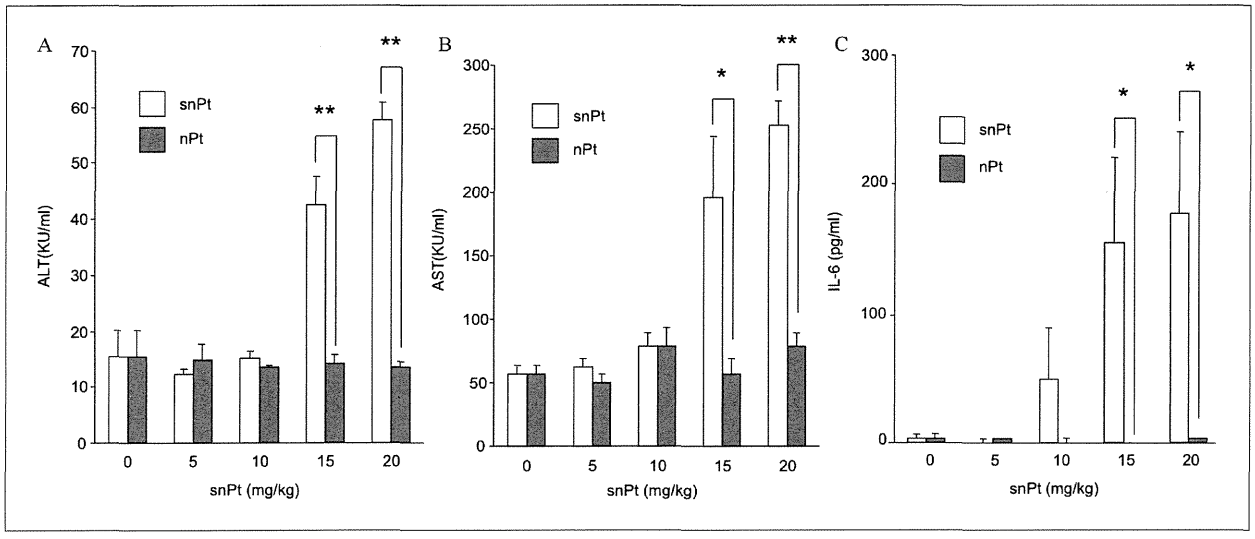

Fig. 5: Effect of particle size of platinum on liver injury. snPt or nPt was intravenously injected into mice at the indicated doses. Blood was recovered at 24 h after injection. Serum ALT (A), AST (B) and IL-6 (C) levels were measured. Data are means ± SEM (n = 3). *Significant difference between the snPt- and nPt-treated groups (*, $p < 0.05$, **, $p < 0.01$)

Acknowledgements: The authors thank all members of our laboratory for useful comments. This study was partly supported by a grant from the Ministry of Health, Labour, and Welfare of Japan.

References

Ai J, Biazar E, Jafarpour M, Montazeri M, Majdi A, Aminifard S, Zafari M, Akbari HR, Rad HG (2011) Nanotoxicology and nanoparticle safety in biomedical designs. Int J Nanomed 6: 1117–1127.

Almeida JP, Chen AL, Foster A, Drezek R (2011) *In vivo* biodistribution of nanoparticles. Nanomedicine (Lond) 6: 815–835.

Ariga K, Hu X, Mandal S, Hill JP (2010) By what means should nanoscaled materials be constructed: molecule, medium, or human? Nanoscale 2: 198–214.

Baughman RH, Zakhidov AA, de Heer WA (2002) Carbon nanotubes–the route toward applications. Science 297: 787–792.

Brabec V, Kasparkova J (2005) Modifications of DNA by platinum complexes. Relation to resistance of tumors to platinum antitumor drugs. Drug Resist Updat 8: 131–146.

Cho WS, Cho M, Jeong J, Choi M, Cho HY, Han BS, Kim HO, Lim YT, Chung BH, Jeong J (2009) Acute toxicity and pharmacokinetics of 13 nm-sized PEG-coated gold nanoparticles. Toxicol Appl Pharmacol 236: 16–24.

Clift MJ, Rothen-Rutishauser B, Brown DM, Duffin R, Donaldson K, Proudfoot L, Guy K, Stone V (2008) The impact of different nanoparticle surface chemistry and size on uptake and toxicity in a murine macrophage cell line. Toxicol Appl Pharmacol 232: 418–427.

Daugaard G (1990) Cisplatin nephrotoxicity: experimental and clinical studies. Dan Med Bull 37: 1–12.

Folkmann JK, Risom L, Jacobsen NR, Wallin H, Loft S, Moller P (2009) Oxidatively damaged DNA in rats exposed by oral gavage to C60 fullerenes and single-walled carbon nanotubes. Environ Health Perspect 117: 703–708.

Furuyama A, Kanno S, Kobayashi T, Hirano S (2009) Extrapulmonary translocation of intratracheally instilled fine and ultrafine particles via direct and alveolar macrophage-associated routes. Arch Toxicol 83: 429–437.

Gehrke H, Pelka J, Hartinger CG, Blank H, Bleimund F, Schneider R, Gerthsen D, Brase S, Crone M, Turk M, Marko D (2011) Platinum nanoparticles and their cellular uptake and DNA platination at non-cytotoxic concentrations. Arch Toxicol 85: 799–812.

Horie M, Kato H, Endoh S, Fujita K, Nishio K, Komaba LK, Fukui H, Nakamura A, Miyauchi A, Nakazato T, Kinugasa S, Yoshida Y, Hagihara Y, Morimoto Y, Iwahashi H (2011) Evaluation of cellular influences of platinum nanoparticles by stable medium dispersion. Metallomics 3: 1244–1252.

Ji Z, Zhang D, Li L, Shen X, Deng X, Dong L, Wu M, Liu Y (2009) The hepatotoxicity of multi-walled carbon nanotubes in mice. Nanotechnology 20: 445101.

Jiang J, Oberdorster G, Elder A, Gelein R, Mercer P, Biswas P (2008) Does Nanoparticle Activity Depend upon Size and Crystal Phase? Nanotoxicology 2: 33–42.

Kajita M, Hikosaka K, Iitsuka M, Kanayama A, Toshima N, Miyamoto Y (2007) Platinum nanoparticle is a useful scavenger of superoxide anion and hydrogen peroxide. Free Radic Res 41: 615–626.

Nabeshi H, Yoshikawa T, Arimori A, Yoshida T, Tochigi S, Hirai T, Akase T, Nagano K, Abe Y, Kamada H, Tsunoda S, Itoh N, Yoshioka Y, Tsutsumi Y (2011) Effect of surface properties of silica nanoparticles on their cytotoxicity and cellular distribution in murine macrophages. Nanoscale Res Lett 6: 93.

Nel A, Xia T, Madler L, Li N (2006) Toxic potential of materials at the nanolevel. Science 311: 622–627.

Nishimori H, Kondoh M, Isoda K, Tsunoda S, Tsutsumi Y, Yagi K (2009) Histological analysis of 70-nm silica particles-induced chronic toxicity in mice. Eur J Pharm Biopharm 72: 626–629.

Nishimori H, Kondoh M, Isoda K, Tsunoda S, Tsutsumi Y, Yagi K (2009) Silica nanoparticles as hepatotoxicants. Eur J Pharm Biopharm 72: 496–501.

Oberdorster G (2010) Safety assessment for nanotechnology and nanomedicine: concepts of nanotoxicology. J Intern Med 267: 89–105.

Oberdorster G, Oberdorster E, Oberdorster J. Nanotoxicology: an emerging discipline evolving from studies of ultrafine particles (2005) Environ Health Perspect 113: 823–839.

Oberdorster G, Sharp Z, Atudorei V, Elder A, Gelein R, Kreyling W, Cox C (2004) Translocation of inhaled ultrafine particles to the brain. Inhal Toxicol 16: 437–445.

Onizawa S, Aoshiba K, Kajita M, Miyamoto Y, Nagai A (2009) Platinum nanoparticle antioxidants inhibit pulmonary inflammation in mice exposed to cigarette smoke. Pulm Pharmacol Ther 22: 340–349.

Park EJ, Kim H, Kim Y, Park K (2010) Intratracheal instillation of platinum nanoparticles may induce inflammatory responses in mice. Arch Pharm Res 33: 727–735.

Patra CR, Bhattacharya R, Mukhopadhyay D, Mukherjee P (2010) Fabrication of gold nanoparticles for targeted therapy in pancreatic cancer. Adv Drug Deliv Rev 62: 346–361.

Pelka J, Gehrke H, Esselen M, Turk M, Crone M, Brase S, Muller T, Blank H, Send W, Zibat V, Brenner P, Schneider R, Gerthsen D, Marko D (2009) Cellular uptake of platinum nanoparticles in human colon carcinoma cells and their impact on cellular redox systems and DNA integrity. Chem Res Toxicol 22: 649–659.

Seglen PO (1976) Preparation of isolated rat liver cells. Methods Cell Biol 13: 29–83.

Service RF. U.S. nanotechnology (2007) Health and safety research slated for sizable gains. Science 315: 926.

Singh S, Shi T, Duffin R, Albrecht C, van Berlo D, Hohr D, Fubini B, Martra G, Fenoglio I, Borm PJ, Schins RP (2007) Endocytosis, oxidative stress and IL-8 expression in human lung epithelial cells upon treatment with fine and ultrafine TiO2: role of the specific surface area and of surface methylation of the particles. Toxicol Appl Pharmacol 222: 141–151.

Watanabe A, Kajita M, Kim J, Kanayama A, Takahashi K, Mashino T, Miyamoto Y (2009) *In vitro* free radical scavenging activity of platinum nanoparticles. Nanotechnology 20: 455105.

Zhu MT, Feng WY, Wang B, Wang TC, Gu YQ, Wang M, Wang Y, Ouyang H, Zhao YL, Chai ZF (2008) Comparative study of pulmonary responses to nano- and submicron-sized ferric oxide in rats. Toxicology 247: 102–111.

blood

2013 121: 2804-2813
Prepublished online January 30, 2013;
doi:10.1182/blood-2012-12-468363

Robo4 is an effective tumor endothelial marker for antibody-drug conjugates based on the rapid isolation of the anti-Robo4 cell-internalizing antibody

Mai Yoshikawa, Yohei Mukai, Yoshiaki Okada, Yuki Tsumori, Shin-ichi Tsunoda, Yasuo Tsutsumi, William C. Aird, Yasuo Yoshioka, Naoki Okada, Takefumi Doi and Shinsaku Nakagawa

Blood (print ISSN 0006-4971, online ISSN 1528-0020), is published weekly by the American Society of Hematology, 2021 L St, NW, Suite 900, Washington DC 20036.

Regular Article

VASCULAR BIOLOGY

Robo4 is an effective tumor endothelial marker for antibody-drug conjugates based on the rapid isolation of the anti-Robo4 cell-internalizing antibody

Mai Yoshikawa,[1] Yohei Mukai,[1,2] Yoshiaki Okada,[1] Yuki Tsumori,[1] Shin-ichi Tsunoda,[2] Yasuo Tsutsumi,[1,2] William C. Aird,[3] Yasuo Yoshioka,[1] Naoki Okada,[1] Takefumi Doi,[1] and Shinsaku Nakagawa[1]

[1]Graduate School of Pharmaceutical Sciences, Osaka University, Osaka, Japan, [2]Laboratory of Biopharmaceutical Research, National Institute of Biomedical Innovation (NiBio), Osaka, Japan, [3]Center for Vascular Biology Research and Division of Molecular and Vascular Medicine, Beth Israel Deaconess Medical Center, Boston, MA

Key Points

- First therapeutic application that targets Robo4 on the tumor blood vasculature
- High-throughput screening system to isolate cell-internalizing monoclonal antibodies useful to develop effective antibody-drug conjugates

Monoclonal antibodies (mAbs) that are internalized into cells are a current focus in the development of antibody-drug conjugates (ADCs). We describe a phage display–based high-throughput screening system to rapidly isolate cell-internalizing mAbs. We simultaneously examined the cell-internalizing activities of several hundred independent mAbs and successfully isolated cell-internalizing mAbs against the tumor endothelial markers Roundabout homolog 4 (Robo4) and vascular endothelial growth factor receptor 2 (VEGFR2). Tumor accumulation of mAbs with high cell-internalizing activity was significantly higher than that of mAbs with low cell-internalizing activity. Furthermore, the antitumor effects of ADCs of mAbs with high cell-internalizing activity were significantly stronger than those of mAbs with low cell-internalizing activity. Although anti-VEGFR2 therapy caused a significant loss of body weight, anti-Robo4 therapy did not. These findings indicate that cell-internalizing activity plays an important role in the biodistribution and therapeutic effects of ADCs. Further, Robo4 can be an effective marker for tumor vascular targeting. (*Blood.* 2013;121 (14):2804-2813)

Introduction

Antibody drug conjugates (ADCs), ie, monoclonal antibodies (mAbs) labeled with certain anticancer agents, are currently the focus of antibody-based drug discovery. ADCs have mAb-derived specificity and allow for targeted delivery of cytotoxic drugs to a tumor, which is expected to significantly enhance the antitumor activity of mAbs.[1] Trastuzumab ematansine (T-DM1)[2] for human epidermal growth factor receptor 2 (Her-2)–positive breast cancer and brentuximab vedotin (SGN-35)[3] for relapsed or refractory CD30-positive lymphoproliferative disorders are now in phase 3 clinical trials as effective ADCs.[4] ADCs will have an important role in overcoming some types of refractory cancers and will contribute to the field of tumor vascular targeting.[5]

An essential property of ADCs is that the mAb should be efficiently internalized into the cell where the cytotoxic effects of anticancer drugs occur.[1] The isolation of mAbs with high cell-internalizing activity (cell-internalizing mAbs) is a limiting factor in the development of ADCs. The discovery of potent cell-internalizing mAbs, however, requires labor-intensive screening of a massive number of candidates, and therefore the development of phage display–based methods to identify these candidates is highly desirable.[6,7] In the phage display–based method, a phage antibody library is added to the desired cells and then phages bound to the cell surface are removed. Only internalized phages are rescued from the intracellular compartment. Even with this method, however, the internalizing activities of individual antibody candidates must be assessed, because the concentrated phage pool comprises a "polyclonal" population. To address this issue, we used high-throughput screening methods to estimate "monoclonal" cell-internalization activities using a protein synthesis inhibitory factor (PSIF),[8] which provided a breakthrough in reducing the time-consuming screening of the cell-internalizing activity.

PSIF is a fragment of a bacterial exotoxin derived from *Pseudomonas aeruginosa*.[9] PSIF lacks its cell binding domain, and its cytotoxic portion is used in a recombinant immunotoxin.[10] Upon entry into the cell, PSIF has strong cytotoxicity by inducing ADP-ribosylation of elongation factor-2, which is essential for protein synthesis.[11] Our group previously accelerated the identification of cell-internalizing novel protein transduction domains (PTDs) by expressing PTD-PSIF fusion proteins in the supernatant of *Escherichia coli*.[8] Using this system, we successfully discovered superior HIV-Tat PTD mutants by simultaneously estimating

Submitted December 3, 2012; accepted January 22, 2013. Prepublished online as *Blood* First Edition paper, January 30, 2013; DOI 10.1182/blood-2012-12-468363.

M.Y. and Y.M. contributed equally to this study.

The online version of this article contains a data supplement.

The publication costs of this article were defrayed in part by page charge payment. Therefore, and solely to indicate this fact, this article is hereby marked "advertisement" in accordance with 18 USC section 1734.

the cell-internalizing activities of several hundred monoclonal PTD-PSIF fusions.[8] Therefore, we expect this method to contribute to the identification of mAbs with high cell-internalizing activity (cell-internalizing mAbs) by expressing single-chain antibody Fv (scFv)-PSIF fusion proteins to estimate the cell-internalizing activities of a very large number of antibodies.

Roundabout homolog 4 (Robo4) is a potential tumor angiogenesis marker.[12] Robo4 expression is restricted to areas of in vivo angiogenesis[13,14] and the subpopulation of hematopoietic stem cells localized in the bone marrow.[15] At angiogenic sites, Robo4 is present in the endothelial lining of blood vessels in the developing embryo,[16] placenta,[14] and tumors.[17] We previously confirmed the endothelial cell–specific expression of Robo4 using transgenic mouse lines.[18,19] Robo4 acts as a receptor that modulates vascular endothelial growth factor A (VEGF)–VEGF receptor (VEGFR) signaling.[20-23] Therefore, Robo4 is a potential marker for tumor vascular targeting because angiogenesis is only activated in tumors in the adult,[24] with the exception of some pathological states.[25,26] Another potential tumor angiogenesis marker is VEGFR2, a well-established tumor endothelial marker.[27] The VEGF-VEGFR2 signaling pathway plays a crucial role in angiogenesis, and anti-VEGF mAbs and small molecule inhibitors against VEGFR are approved for various types of cancers.[28] Anti-VEGFR2 mAbs are also used for tumor vascular targeting.[29] Although VEGFR2 is strongly expressed in active angiogenic sites, its expression is also observed in normal tissues.[30] Hypertension and proteinuria are common side effects of anti-VEGF therapy because VEGF-VEGFR signaling is also inhibited in normal tissue, including the kidney, heart, and resistance vessels.[31-33]

Here we applied the PSIF system to search for novel cell-internalizing mAbs from an immune phage antibody library. Application of this method to Robo4 and VEGFR2 led to the successful discovery of anti-Robo4 and anti-VEGFR2 cell-internalizing mAbs, as well as mAbs with low cell-internalizing activity (low-internalizing mAbs) to be used as controls. Comparing mAbs with different cell-internalizing activities revealed that higher cell-internalizing activity enhanced the tumor targeting potency of mAbs. Furthermore, comparative studies with anti-Robo4 and anti-VEGFR2 cell-internalizing mAbs in vivo indicated that Robo4 was superior to VEGFR2 in terms of the therapeutic window. This is the first report demonstrating the benefits of cell-internalizing mAbs in tumor vascular targeting. Further, these findings demonstrate the potential of Robo4 as a target for further development of novel ADCs against tumor blood vasculature.

Materials and methods

Cell culture

MS1 immortalized murine endothelial cells were cultured in Dulbecco's Modified Eagle Medium containing 5% fetal bovine serum 1% antibiotic-antimycotic mixed solution. B16BL6 murine melanoma cells were cultured in minimum essential medium containing 10% fetal bovine serum and 1% antibiotic-antimycotic mixed solution at 37°C. These cells were maintained at 37°C under a humidified 5% CO_2 atmosphere.

B16BL6 tumor-bearing mice

B16BL6 cells (1×10^6 cells/100 μL) were inoculated intracutaneously into 6-week-old female C57BL6 mice (Japan SLC Inc., Shizuoka, Japan) (day 0). Biodistribution was analyzed on the day that the tumor width reached 10 mm. The therapy experiment was started on day 3. As a validation of the model, we confirmed the expressions of VEGFR2 and Robo4 on the tumor endothelium, based on the immunofluorescence against B16BL6 tumor sections.

Antigens

Human VEGFR2 (hVEGFR2) and mouse VEGFR2 (mVEGFR2) were commercial recombinant proteins (Merck Chemicals, Inc., Darmstadt, Germany, or R&D Systems, Inc., Minneapolis, MN). Human Robo4 (hRobo4) and mouse Robo4 (mRobo4) were produced as described previously.[34]

Immune phage antibody libraries

Phage antibody libraries were constructed from the spleen and bone marrow cells of immunized mice as previously described.[35,36] Our phage antibody library comprised single-chain Fv fragment (scFv) fused with pIII phage coat protein. Four rounds of affinity panning were performed against hVEGFR2 and mVEGFR2 for the anti-VEGFR2 immune library, and against hRobo4 and mRobo4 for the anti-Robo4 immune library. Anti-FLAG panning was followed by each panning to concentrate the scFv-displaying phages, as described previously.[36]

ELISA and cytotoxicity assay using TG1 supernatant

Plasmids were extracted from TG1 cells after the fourth panning against mVEGFR2 or mRobo4. These "enriched" scFv gene libraries were cloned into a PSIF-fusion expression vector derived from pCANTAB5E.[8] Monoclonal scFv-PSIF protein was induced in the TG1 supernatant, as previously described.[8] mVEGFR2 or mRobo4 was immobilized on an immunoassay plate and blocked with 4% skim milk in phosphate-buffered saline (PBS) (4% MPBS) at 37°C for 2 hours. TG1 supernatant containing 2% MPBS was reacted with antigens at room temperature for 1 hour. Bound scFv-PSIFs were detected by anti–FLAG-horseradish peroxidase (M2, Sigma-Aldrich Corporation, St. Louis, MO). For the cytotoxicity assay, MS1 cells were seeded on a 96-well plate at 1.0×10^4 cells/well. After incubation at 37°C for 24 hours, TG1 supernatant was diluted in MS1 culture medium, and then added to the MS1 cells. After incubation at 37°C for 24 hours, cell viability was assessed using a WST-8 assay (Dojindo Molecular Technologies, Inc., Kumamoto, Japan). The viability of nontreated MS1 and completely killed MS1 with 1 mM cycloheximide were defined as 100% and 0%, respectively.

Expression and purification of scFv, dscFv, and scFv-PSIF recombinant protein

The isolated scFv gene with 15 amino acids linker (VL-GGGGSGGG GSGGGGS-VH) was cloned into modified pET15b vector, resulting in the scFv fused by FLAG-tag and His×6 tag at the C-terminus. A scFv gene with a 5–amino acid linker (VL-GGGGS-VH) was also cloned into modified pET15b, resulting in a noncovalent scFv dimer (dscFv) fused by FLAG-tag and His×6 tag at the C-terminus. An anti-His scFv gene was also cloned but only a FLAG-tag was fused at the C-terminus. A scFv gene with a 15–amino acid linker was cloned into pYas-PSIF vectors.[37] ScFvs, dscFvs, and scFv-PSIFs were purified from inclusion bodies in *E coli* according to the previously described methods.[37] The binding affinity of each recombinant protein was assessed by surface plasmon resonance using BIAcore3000 (GE Healthcare UK Ltd., Chalfont, United Kingdom).

Expression and purification of IgG recombinant protein

IgG recombinant proteins were expressed using an OptiCHO antibody expression kit (Invitrogen Corporation, Carlsbad, CA) according to the manufacturer's instructions. IgGs were purified from cell culture supernatant with protein G column (GE Healthcare). Eluted fractions were further purified with Superdex 200 column (GE Healthcare). Anti-FLAG[IgG] (anti-FLAG M2 antibody) was purchased from Sigma-Aldrich.

Preparation of IgG-NCS

NCS was kindly provided by Kayaku Co, Ltd., Tokyo, Japan. NCS was thiolated by incubating it with 10 molar excess 2-iminothiolane (Thermo Fisher Scientific Inc., Waltham, MA) for 1 hour at room temperature. IgG recombinant proteins were reacted with 10 molar excess of SPDP

crosslinker (*N*-succinimidyl 3-[2-pyridyldithio]-propionate; Thermo Fisher) for 30 minutes on ice. SPDP-modified IgGs and thiolated NCS were separately purified using NICK columns (GE Healthcare). They were then mixed for 8 hours at room temperature. IgG-NCS were purified with a Superdex 200 column. Modification efficiency was quantified after sodium-dodecyl sulfate-polyacrylamide gel electrophoresis using a Gel DOC EZ system and Image laboratory software (Bio-Rad Laboratories, Inc., Hercules, CA).

Labeling of purified mAbs

For fluorescent labeling, mAbs were labeled using Cy5.5-NHS (GE Healthcare). For ^{125}I labeling, 100 μg mAbs in 0.4 M phosphate buffer were labeled with 0.2 mCi Na^{125}I (PerkinElmer, Inc., Waltham, MA) based on the chloramine-T method.[38] For biotin labeling, mAbs were biotinylated using EZ-Link Sulfo-NHS-Biotin (Thermo Fisher). Each mAb was purified using a NICK desalting column (GE Healthcare).

Flow cytometry

Cy5.5-labeled mAb ($mAb^{Cy5.5}$; 4 μM) was incubated with 5.0×10^5 cells of MS1 cells in 6-well plates for 2 hours at 4°C. After washing three times, the cells were incubated for an additional 0.5 to 8 hours at 37°C. At each time point, cells were collected in 2-mM ethylenediaminetetraacedtic acid/PBS. Bound mAbs were digested using 0.1% trypsin/PBS at 37°C for 20 minutes (trypsinized group) or PBS (nontrypsinized group). Cellular fluorescence was measured by Gallios flow cytometer (Beckman Coulter, Inc., Miami, FL). The ratio of internalization was calculated using the following formula: internalization (%) = {internalized $mAb^{Cy5.5}$}/{total bound $mAb^{Cy5.5}$} × 100 (%) = {(MFI of $mAb)_T$ − (MFI of anti-His $[mAb])_T$}/{(MFI of $mAb)_N$ − (MFI of anti-His$[mAb])_N$} × 100 (%). MFI indicates mean fluorescence intensity. T and N indicate trypsinized and nontrypsinized groups, respectively.

In vivo biodistribution

$dscFvs^{125I}$ (0.2 nmol) was intravenously injected into B16BL6 tumor–bearing mice. At 2 hours and 24 hours after injection, the radioactivity of each organ was counted using the Wizard 2480 γ-ray counter (PerkinElmer). %ID/g tissue was calculated using following formula: %ID/g tissue = (count/g tissue)/(total injected count) × 100 (%). Two individual experiments were combined for the final data (total 11 mice/group).

Immunofluorescence of the tissue sections

B16BL6 tumor–bearing mice were administered 2 nmol of $dscFvs^{Bio}$. At 2 hours after the injection, the tumors, kidneys, and hearts were embedded in optimal cutting temperature compound (Sakura Finetek, Inc., Torrance, CA) and frozen in liquid nitrogen. Thin sections (7 μm) were prepared using a Cryostat CM1850 (Leica Microsystems GmbH, Wetzlar, Germany) and fixed in 4% paraformaldehyde. $DscFvs^{Bio}$ in the sections were stained with streptavidin phycoerythrin conjugate (eBioscience Inc., San Diego, CA) in Dako REAL Antibody Diluent (DAKO Corporation, Carpinteria, CA). CD31+ vascular endothelial cells were stained with rat anti-CD31 antibody (MEC13.3; Becton Dickinson and Company, Franklin Lakes, NJ) in Dako REAL Antibody Diluent and Alexa488 conjugated anti-rat IgG (A11006; Invitrogen). The samples were embedded with Prolong Gold antifade reagent with 4′,6-diamidino-2-phenylindole (Invitrogen) and observed with a fluorescence microscope FSX100 (Olympus Corporation, Tokyo, Japan).

In vivo therapy experiments

Activities of scFv-PSIFs and IgG-NCSes were confirmed by WST-8 assay as described before. B16BL6 cells were inoculated intracutaneously into C57BL6 mice (Japan SLC) on day 0. Mice were intravenously injected with 15 pmol scFv-PSIFs and 10 pmol IgG-NCSs on days 3, 5, 7, 9, and 11 (7 mice/group). The volume of the tumor was calculated according to the following formula: tumor volume (mm^3) = {major axis of tumor (mm)} × {minor axis of tumor (mm)}^{2} × 0.4.

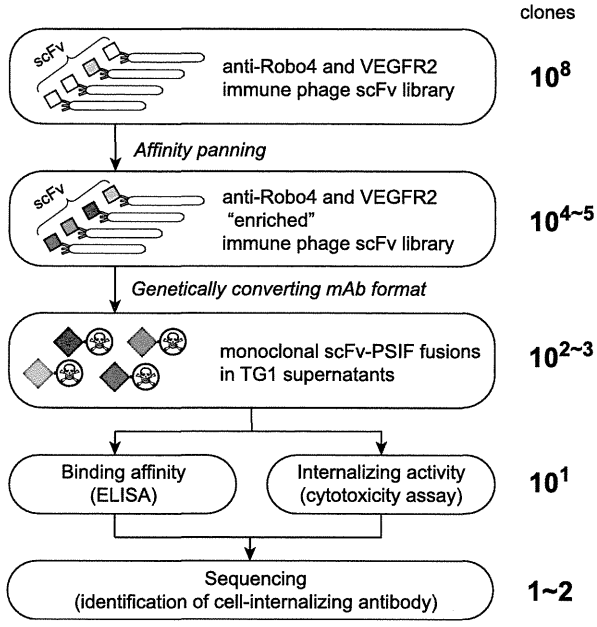

Figure 1. Phage display-based method to search for cell-internalizing mAbs. The phage antibody library was "enriched" by affinity panning against the desired antigens. Plasmids encoding scFvs were collected from TG1 *E coli* strains infected by "enriched" phage libraries. Genes of scFvs were digested out and ligated into a PSIF fusion protein expression vector. These plasmids were then transformed to TG1, and then single colonies were picked up. From these individual colonies, monoclonal scFv-PSIF fusions were induced in TG1 supernatants. Using these fusion proteins, binding affinities and internalizing activities of several hundreds of scFv-PSIFs were easily estimated by ELISA and cytotoxicity assays, respectively. Finally, genes of positive scFvs were collected from TG1, and cell-internalizing scFvs were identified by sequencing. In this report, we used anti-Robo4 and anti-VEGFR2 immune phage scFv libraries as the phage antibody libraries, and mRobo4 and mVEGFR2 as the desired antigens.

Results

High-throughput screening for cell-internalizing mAbs

To identify cell-internalizing mAbs, we applied the phage immune scFv library to high-throughput screening of cell-internalizing molecules based on the PSIF system[8] (Figure 1). Our anti-Robo4 or anti-VEGFR2 phage library comprised approximately 3.0×10^8 or 5.0×10^8 independent scFvs, which was validated by sequence analysis. To assess the qualities of the libraries, affinity panning was performed against each antigen. During the panning, output phages were increased, suggesting that the desired scFvs were enriched in the library (supplemental Figure 1A-B,E-F). After the fourth panning, >40% of monoclonal scFvs showed specific binding in enzyme-linked immunosorbent assay (ELISA) (supplemental Figure 1C-D,G-H).

To validate the efficacy of cell-internalizing mAbs in a mouse model, we selected libraries enriched against murine antigens (mRobo4 and mVEGFR2) and chose MS1 murine endothelial cells for the screening of cell-internalizing mAbs because we confirmed the expressions of both mRobo4 and mVEGFR2 in MS1 cells using reverse transcriptase–polymerase chain reactioin. For the screening, scFv genes obtained after the fourth round of panning were cloned into the PSIF expression vector. Monoclonal scFv-PSIFs were expressed in TG1 supernatants (315 clones per library). For anti-Robo4s, 178 of 315 clones bound to mRobo4 in ELISA and 20 of these 178 binders were cytotoxic against MS1 cells

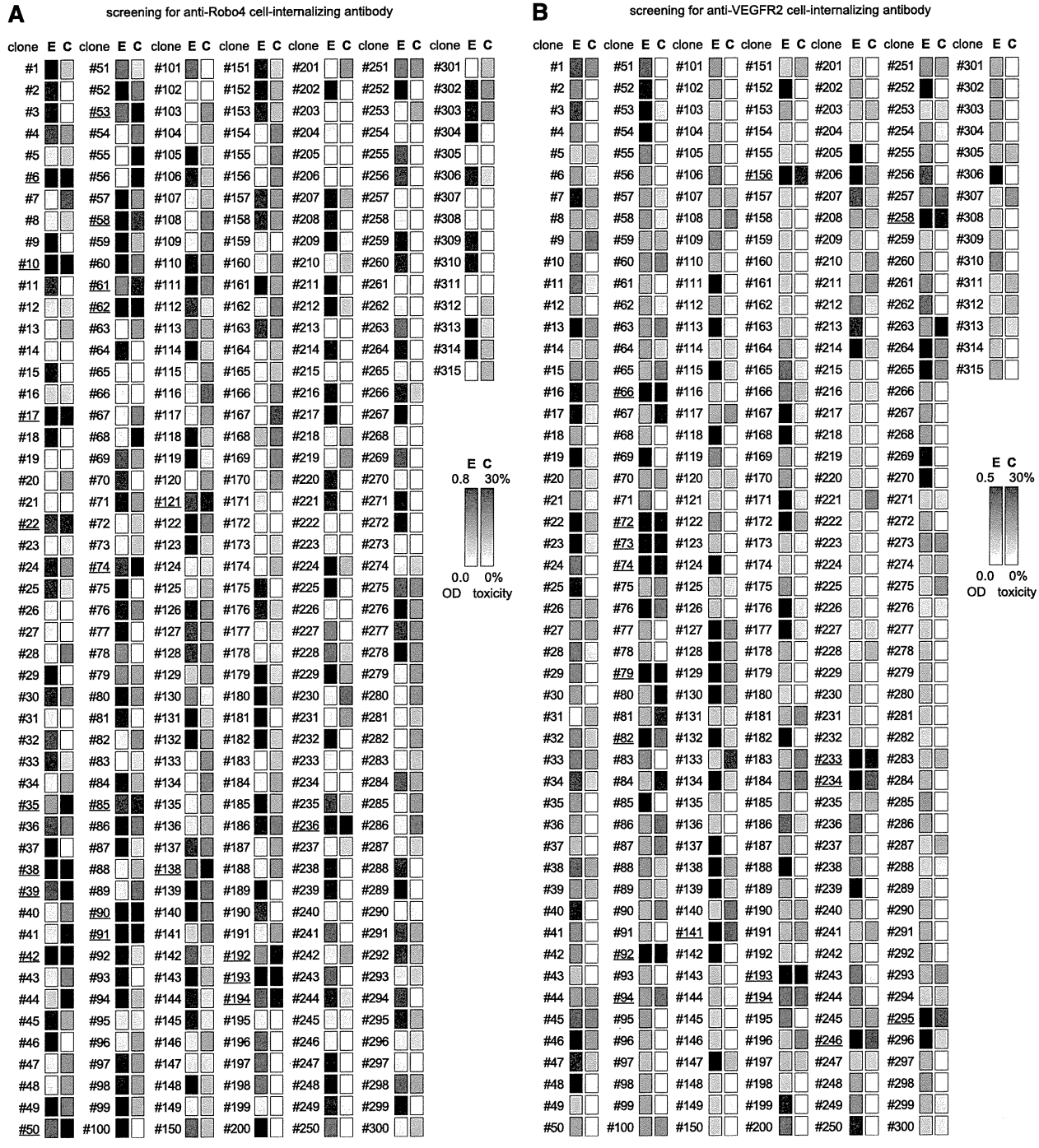

Figure 2. Screening of cell-internalizing mAbs (ELISA and cytotoxicity assay). To screen for cell-internalizing mAbs, 315 clones per antigen were analyzed by ELISA and cytotoxicity assay. (A) Result for Robo4, (B) Result for VEGFR2. Monoclonal scfv-PSIFs were induced in TG1 supernatant. The binding properties and cytotoxicities to MS1 cells were then assessed by an ELISA and WST-8 assay, respectively. E, ELISA results; C, WST-8 assay results. Individual results from ELISA (OD = 0.8 or 0.5~0.0) and WST-8 assay (cytotoxicity = 30%~0%) were mapped in grayscale densities. The 24 candidates against Robo4 and 17 candidates against VEGFR2 are indicated by the underline (ELISA OD ≥0.2 and cytotoxicity ≥20%). After omitting redundant clones by sequencing, 1 cell-internalizing mAb and 2 low-internalizing mAbs against mRobo4, and 2 cell-internalizing mAbs and 14 low-internalizing mAbs against mVEGFR2 were identified.

(Figure 2A). In a similar manner, for anti-VEGFR2s, 156 of 315 clones bound to VEGFR2 and 17 of the 156 binders were positive in the ELISA and cytotoxicity assays (Figure 2B). Sequence analysis to omit redundant clones revealed that these clones comprised 1 anti-Robo4 cell-internalizing mAb, 2 anti-Robo4 low-internalizing mAbs, 2 anti-VEGFR2 cell-internalizing mAbs, and 14 anti-VEGFR2 low-internalizing mAbs. For anti-Robo4s, only one anti-Robo4 cell-internalizing mAb was named "R4-13i" and a low-internalizing mAb with high affinity and low cytotoxicity was named "R4-16." In a similar manner, "V2-05i" and "V2-02" were selected as an anti-VEGFR2 cell-internalizing mAb and a low-internalizing mAb, respectively. After purification of the recombinant proteins, both anti-Robo4 scFvs bound to hRobo4, similar to mRobo4. Conversely, anti-VEGFR2 scFvs bound to

Table 1. Binding kinetics of antibodies in surface plasmon resonance analysis

Antibody	Target	Format	k_a ($M^{-1}s^{-1}$)	k_d (s^{-1})	K_D (M)
R4-13i	mRobo4	scFv	$1.25 \pm 0.36 \times 10^5$	$5.82 \pm 0.95 \times 10^{-4}$	$5.03 \pm 1.95 \times 10^{-9}$
(internalizing)		dscFv	$1.15 \pm 0.34 \times 10^6$	$5.98 \pm 0.61 \times 10^{-4}$	$5.64 \pm 2.21 \times 10^{-10}$
		IgG	$1.14 \pm 0.55 \times 10^6$	$4.19 \pm 1.70 \times 10^{-4}$	$2.22 \pm 0.51 \times 10^{-10}$
		scFv-PSIF	$7.22 \pm 4.31 \times 10^4$	$4.28 \pm 1.60 \times 10^{-3}$	$6.47 \pm 1.61 \times 10^{-8}$
		IgG-NCS	$1.02 \pm 0.15 \times 10^6$	$4.66 \pm 0.86 \times 10^{-4}$	$4.59 \pm 0.74 \times 10^{-10}$
R4-16	mRobo4	scFv	$1.30 \pm 0.33 \times 10^5$	$5.82 \pm 1.50 \times 10^{-4}$	$4.77 \pm 1.96 \times 10^{-9}$
(low-internalizing)		dscFv	$1.12 \pm 0.03 \times 10^6$	$5.91 \pm 1.50 \times 10^{-4}$	$5.31 \pm 1.96 \times 10^{-10}$
		IgG	$1.06 \pm 0.24 \times 10^6$	$3.60 \pm 0.85 \times 10^{-4}$	$2.76 \pm 0.16 \times 10^{-10}$
		scFv-PSIF	$8.90 \pm 1.42 \times 10^4$	$6.10 \pm 2.45 \times 10^{-3}$	$7.24 \pm 3.74 \times 10^{-8}$
		IgG-NCS	$1.07 \pm 0.12 \times 10^6$	$3.93 \pm 0.54 \times 10^{-4}$	$3.72 \pm 0.89 \times 10^{-10}$
V2-05i	mVEGFR2	scFv	$9.66 \pm 3.57 \times 10^4$	$4.40 \pm 0.95 \times 10^{-4}$	$5.13 \pm 2.61 \times 10^{-9}$
(internalizing)		dscFv	$8.75 \pm 2.03 \times 10^5$	$5.59 \pm 2.57 \times 10^{-4}$	$6.16 \pm 1.47 \times 10^{-10}$
		IgG	$1.14 \pm 0.09 \times 10^6$	$3.21 \pm 0.35 \times 10^{-4}$	$2.84 \pm 0.52 \times 10^{-10}$
		scFv-PSIF	$9.57 \pm 0.84 \times 10^4$	$6.51 \pm 1.87 \times 10^{-3}$	$6.94 \pm 2.63 \times 10^{-8}$
		IgG-NCS	$0.96 \pm 0.06 \times 10^6$	$4.37 \pm 0.90 \times 10^{-4}$	$4.52 \pm 0.79 \times 10^{-10}$
V2-02	mVEGFR2	scFv	$7.94 \pm 1.24 \times 10^4$	$4.28 \pm 3.23 \times 10^{-4}$	$5.07 \pm 3.05 \times 10^{-9}$
(low-internalizing)		dscFv	$8.94 \pm 2.55 \times 10^5$	$5.57 \pm 1.25 \times 10^{-4}$	$6.60 \pm 2.39 \times 10^{-10}$
		IgG	$1.13 \pm 0.22 \times 10^6$	$3.25 \pm 1.10 \times 10^{-4}$	$2.90 \pm 0.98 \times 10^{-10}$
		scFv-PSIF	$9.84 \pm 1.52 \times 10^4$	$5.75 \pm 2.05 \times 10^{-3}$	$5.81 \pm 1.93 \times 10^{-8}$
		IgG-NCS	$1.08 \pm 0.08 \times 10^6$	$5.25 \pm 1.58 \times 10^{-4}$	$4.85 \pm 1.30 \times 10^{-10}$

Binding kinetics were analyzed against mRobo4 (R4-13i and R4-16) or mVEGFR2 (V2-05i and V2-02). Values are shown as means ± SD from three different preparations.

k_a, association rate constant ($M^{-1}s^{-1}$); k_d, dissociation rate constant (s^{-1}); K_D, equilibrium dissociation constant (k_d/k_a) (M).

mVEGFR2, but not to hVEGFR2. We also confirmed using competitive ELISA that the mAbs did not share their antigen-binding epitopes (supplemental Figure 2).

Characterization of mAbs

We purified scFvs, dimerized scFvs (dscFvs), IgGs, and scFv-PSIF as recombinant proteins. IgGs conjugated with neocarzinostatin (IgG-NCSes) were also prepared for in vivo experiments. NCSes were confirmed to be conjugated to IgG molecules in the purified IgG-NCS fraction, and the efficiencies of the NCS modifications were similar in all IgG-NCSes (1.6~1.8 NCSes per single IgG). Surface plasmon resonance analysis revealed that cell-internalizing mAbs and low-internalizing mAbs had similar affinities against antigens in all antibody forms (Table 1).

To quantify the internalization, flow cytometry analysis was performed with Cy5.5-labeled mAbs ($scFv^{Cy5.5}$, $dscFv^{Cy5.5}$, and $IgG^{Cy5.5}$; Figure 3A,C). After $mAbs^{Cy5.5}$ bound to the cell surface, internalization was induced by incubation at 37°C for 2 hours. By removing cell-surface $mAbs^{Cy5.5}$ with trypsinization, the internalized $mAbs^{Cy5.5}$ were quantified by flow cytometry. At 2 hours, approximately 30% of cell-internalizing mAbs remained after trypsinization, whereas most of the low-internalizing mAbs were degraded (Figure 3A,C). This result clearly suggested that the internalization efficiencies differed between cell-internalizing mAbs and low-internalizing mAbs, even among the three different mAb forms. In a similar manner, a time-shift analysis revealed that >40% of cell-internalizing mAbs were internalized after 8 hours of incubation (Figure 3B,D). These findings indicate that only cell-internalizing mAbs were efficiently internalized into the cells, although low-internalizing mAbs had affinities similar to those of cell-internalizing mAbs (Table 1).

Intracellular localization

The intracellular behaviors of cell-internalizing mAbs were analyzed with a confocal laser-scanning microscope. In MS1 cells, intracellular fluorescence derived from $scFv^{Cy5.5}$ was observed with cell-internalizing scFvs, but not with low-internalizing scFvs (supplemental Figure 3A,D,E,H). Fluorescence was suppressed, however, under the inhibition of energy-dependent endocytosis (supplemental Figure 3B-C,F-G). These results suggested that cell-internalizing scFvs entered into the cells via energy-dependent endocytosis.

For in-depth analysis of the intracellular behavior, confocal laser-scanning microscope analysis was performed with immunostaining of endosome markers (supplemental Figure 3Iab). After $scFvs^{Cy5.5}$ were bound to the cell-surface, the cells were incubated for an additional 1 to 8 hours at 37°C. The early endosome marker, early endosome antigen 1 (EEA1), and the late endosome marker, lysosomal-associated membrane protein 1 (LAMP1), were visualized using Alexa488-conjugated antibodies. Colocalization with EEA1+ early endosomes decreased over time (supplemental Figure 3I-M,S-W), whereas colocalization with LAMP1+ late endosomes increased (supplemental Figure 3N-R,Xab). These findings suggested that cell-internalizing scFvs were encapsulated in EEA1+ early endosomes at an early stage and eventually accumulated in LAMP1+ late endosomes. This is thought to be a typical endocytotic molecular sorting pathway.[39]

Influence of cell-internalizing activity on biodistribution

To assess the biodistribution of cell-internalizing mAbs, ^{125}I-labeled dscFvs ($dscFv^{125I}$) were intravenously injected into B16BL6 tumor-bearing mice. In this experiment, we selected the dscFv form because dscFv has superior in vivo tumor-targeting potency compared with scFv.[40] At 2 hours, the tumor distribution of anti-Robo4 and anti-VEGFR2 $dscFvs^{125I}$ was similar to but significantly higher than that of a negative control $dscFv^{125I}$ (anti-His[dscFv]^{125I}; Figure 4A-B). This finding suggested that the anti-Robo4 and anti-VEGFR2 dscFvs had tumor-targeting properties. Anti-Robo4 $dscFvs^{125I}$ also accumulated in the kidney, indicating a nonspecific distribution of dscFvs for their elimination,[41,42] because no significant difference was observed between anti-Robo4 $dscFvs^{125I}$

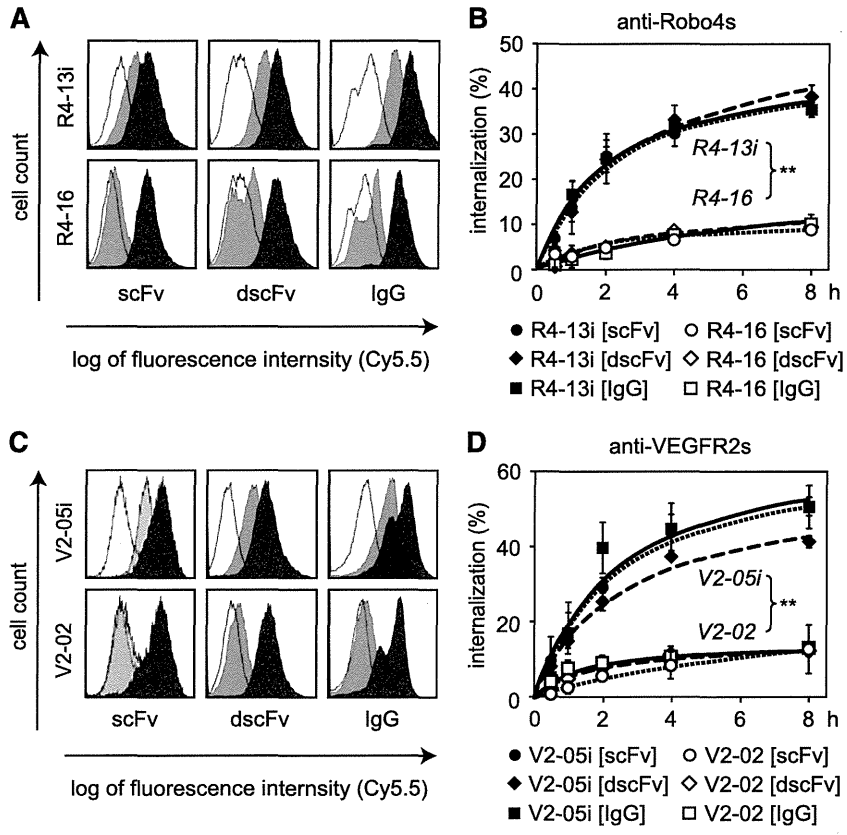

Figure 3. Cell internalization analyzed by flow cytometry. (A,C) Trypsinization to quantify internalized mAbs. Different forms of $mAbs^{Cy5.5}$ bound to the MS1 cells at 4°C. After washing out the unbound mAbs, internalization was induced for 2 hours at 37°C. To detect only internalized mAbs, cell surface proteins were trypsinized. The remaining cellular fluorescence was then analyzed by flow cytometry. (A) Anti-Robo4 $mAbs^{Cy5.5}$, (C) Anti-VEGFR2 $mAbs^{Cy5.5}$. Black, nontrypsinized group; gray, trypsinized group; white, negative control (anti-His[scFv]$^{Cy5.5}$, anti-His[dscFv]$^{Cy5.5}$, or anti-FLAG [IgG]$^{Cy5.5}$). (B,D) Time course of the internalization. After binding at 4°C, internalization was induced for 0.5, 1, 2, 4, or 8 hours at 37°C. The ratio of internalization was calculated using the following formula: internalization (%) = {*internalized mAb*}/{*total bound mAb*} × 100 (%) = {(MFI of mAb)$_T$ − (MFI of negative control)$_T$}/{(MFI of mAb)$_N$ − (MFI of negative control)$_N$} × 100 (%). T, trypsinized group; N, nontrypsinized group; MFI, mean fluorescence intensity. (B) Closed and open markers indicate R4-13i and R4-16, respectively. (D) Closed and open markers indicate V2-05i and V2-02, respectively. (B,D) Circles, diamonds, and squares indicate scFv, dscFv, and IgG, respectively. Each experiment was performed in triplicate. Values are shown as means ± SD. $^{**}P < .01$; internalizing mAb versus low-internalizing mAb in each form by 2-way ANOVA (n = 3).

and anti-His[dscFv]^{125I} (Figure 4A). Importantly, the accumulation of anti-VEGFR2 $dscFvs^{125I}$ in the kidney was significantly greater than that of anti-His[dscFv]^{125I} (Figure 4B). A similar accumulation of anti-VEGFR2 $dscFvs^{125I}$, but not anti-Robo4 $dscFvs^{125I}$ (Figure 4A), was observed in the heart (Figure 4B).

To confirm this phenomenon, the localization of dscFvs in the tissues was analyzed by immunofluorescence studies (Figure 4E-S). Biotin-labeled dscFvs ($dscFvs^{Bio}$) were intravenously administered to B16BL6 tumor–bearing mice and the tumors, kidneys, and hearts were extracted 2 hours after injection. The $dscFv^{Bio}$ and vascular endothelial cells were stained by streptavidin-AP and anti-CD31 antibody, respectively. In the tumor sections, all of the anti-Robo4 and anti-VEGFR2 $dscFvs^{Bio}$ were clearly detected with CD31+ tumor blood vasculature, whereas anti-His[dscFv]^{Bio} was not detectable (Figure 4E,H,K,N,Q). This finding suggested that both anti-Robo4 and anti-VEGFR2 dscFvs recognized tumor endothelial cells in vivo, which contributed to their accumulation in the tumor. Interestingly, in the kidney and heart sections, signals around CD31+ blood vasculature were detectable only with the anti-VEGFR2 $dscFvs^{Bio}$, and not with anti-Robo4 $dscFvs^{Bio}$ or anti-His[dscFv]^{Bio} (Figure 4F-G,I-J,L-M,O-P,R-S). This finding was compatible with the biodistribution results (Figure 4A-B), which suggested that anti-VEGFR2 dscFvs recognized VEGFR2 on normal blood vessels because VEGFR2 plays an important role in normal tissues, including the kidney and heart.[31-33] No specific accumulation of anti-Robo4 dscFvs was observed in normal tissues, suggesting that the anti-Robo4 mAbs were useful for specific tumor vascular targeting.

Comparison of the cell-internalizing mAbs and low-internalizing mAbs revealed a significantly greater accumulation of cell-internalizing $dscFvs^{125I}$ in the tumors compared with low-internalizing $dscFvs^{125I}$ at 24 hours (Figure 4C-D), whereas no differences were observed at 2 hours (Figure 4A-B). This finding suggested that cell-internalizing mAbs were retained in the tumor for a longer time than the low-internalizing mAbs. This phenomenon was also observed in the kidney and heart with the anti-VEGFR2 dscFvs (Figure 4D). This retention might be caused by the mAb internalization, which allowed the mAb to escape from the bloodstream and accumulate in the tumor blood endothelial cells. Taken together, these results suggest that mAb internalization into the tumor endothelium improves mAb-based drug-delivery in vivo.

Enhanced antitumor effect depends on the cell-internalizing activity

To assess the antitumor potencies of the cell-internalizing mAbs, we selected the scFv-PSIF and IgG-NCS forms. Both forms were suitable models of ADCs because both drugs are used clinically as successful anticancer medicines.[10,43] First, the in vitro cell-killing activities of scFv-PSIFs and IgG-NCSes were estimated by a cytotoxicity assay with MS1 cells (Figure 5A-D). Both forms of cell-internalizing mAbs showed an approximately 10-fold higher cytotoxicity than the low-internalizing mAbs. These findings clearly suggest that internalization enhanced the delivery of conjugated drugs into the cells because our cell-internalizing mAbs and low-internalizing mAbs had similar affinities against antigens (Table 1).

As the therapy experiment in vivo, scFv-PSIFs and IgG-NCSes were intravenously injected into B16BL6 tumor–bearing mice once every 2 days for a total of 5 injections (Figure 5E-H). All cell-internalizing mAbs significantly suppressed tumor growth, whereas the antitumor effects of the low-internalizing antibodies were

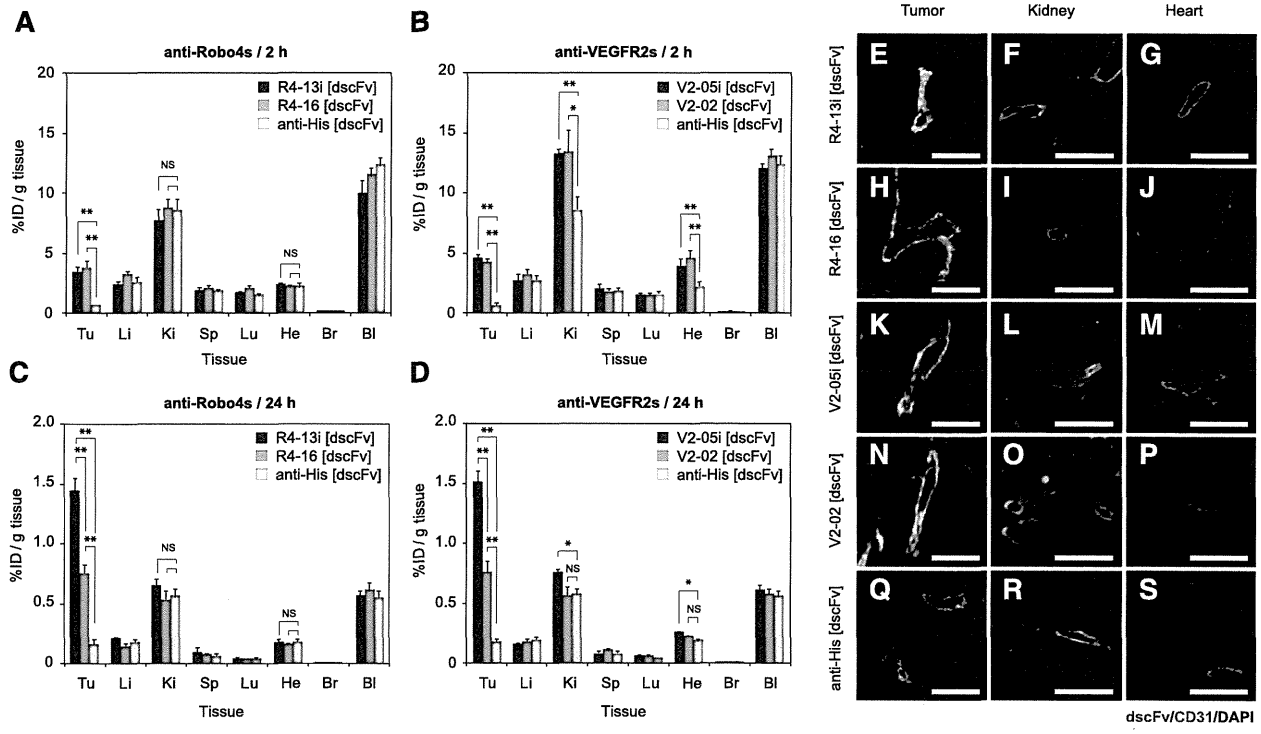

Figure 4. In vivo tumor-targeting activity of cell-internalizing mAbs. (A-D) Biodistribution of dscFvs in B16BL6 tumor–bearing mice. B16BL6 tumor–bearing mice were intravenously administered with anti-Robo4 dscFvs^{125I} (A,C) or anti-VEGFR2 dscFvs^{125I} (B,D). Each organ was extracted after 2 hours (A,B) or 24 hours (C,D), and the radioactivity was measured using a γ counter. %ID/g tissue was calculated using the following formula: %ID/g tissue = (count/g tissue)/(total injected count) × 100 (%). Tu, tumor; Li, liver; Ki, kidney; Sp, spleen; Lu, lung; He, heart; Br, brain; Bl, blood. (A,C) black; R4-13i[dscFv]^{125I}; gray, R4-16[dscFv]^{125I}; white, anti-His[dscFv]^{125I}. (B,D) black, V2-05i[dscFv]^{125I}; gray, V2-02[dscFv]^{125I}; white, anti-His[dscFv]^{125I}. Values are shown as means ± SEM. $^*P < .05$; $^{**}P < 0.01$; NS, not significant in Student's *t*-test (n = 11). (E-S) Co-immunostaining of dscFvs with CD31$^+$ blood endothelial cells on the tissue section. B16BL6 tumor–bearing mice were intravenously administered dscFvs^{Bio}. The tumor, kidney, and heart were extracted after 2 hours. Tissue sections of tumor, kidney, and heart were stained with streptavidin-PE conjugate. The blood vasculature was also stained with anti-CD31 antibody. Images were digitally merged. Red, dscFv^{Bio}; green, CD31; blue, DAPI (nucleus); yellow, colocalized region of red and green. Scale bar represents 100 μm. (E-G) R4-13i[dscFv]; (H-J) R4-16[dscFv]; (K-M) V2-05i[dscFv]; (N-P) V2-02[dscFv]; (Q-S) anti-His[dscFv]. (E,H,K,N,Q) Tumor section, (F,I,L,O,R) kidney section, and (G,J,M,P,S) heart section.

similar to those of the negative controls (anti-His[scFv]-PSIF and anti-FLAG[IgG]-NCS). The antitumor effects of R4-13i and V2-05i were similar in both ADC forms. These findings strongly suggest that the cell-internalizing activity of the mAbs was essential to maximize the delivery of the conjugated drug into the target cells, which significantly enhanced the antitumor effect of the ADCs.

Interestingly, the group of mice administered V2-05i[scFv]-PSIF had a significant loss of body weight, whereas the other groups did not (Figure 5I-L). As a preliminary result, 6 of 7 mice died in the V2-05i[scFv]-PSIF group with a similar protocol but with a fourfold higher dosage (60 pmol/mouse), perhaps because of the disruption of VEGFR2-positive cells in normal tissues by V2-05i[scFv]-PSIF, as shown in Figure 4. This side effect was not observed in the V2-05i [IgG]-NCS group. Therefore, we also hypothesized that the toxicity of NCS in normal cells was weak because NCS inhibits DNA synthesis in growing cells, such as tumor cells.[44] At a higher dosage, however, V2-05i[IgG]-NCS carries the risk of side effects. With regard to this point, none of the anti-Robo4 ADCs induced a loss of body weight; therefore, we concluded that Robo4 is a potential target for tumor vascular targeting with ADC.

Discussion

This study led to three novel findings. First, we demonstrated a rapid screening system for cell-internalizing mAbs in combination with the phage antibody library, which accelerated the identification of desired cell-internalizing mAbs. Second, comparative in vivo studies using cell-internalizing mAbs and low-internalizing mAbs with the same affinity values revealed that mAb internalization contributed to tumor targeting and enhanced the antitumor effects of the ADCs. Third, the first in vivo therapeutic application with anti-Robo4 mAb revealed that Robo4 is a therapeutic target on the tumor endothelial cells. The first and second findings will greatly contribute to the development of antibody therapies based on cell-internalizing antibodies such as ADCs, targeted liposomal drugs, or imaging. The third finding provides a new focus regarding the role of Robo4 biology in the body, such as the decreased side effects associated with depleting Robo4-positive endothelial cells in vivo.

This method allowed us to successfully isolate anti-Robo4 and anti-VEGFR2 cell-internalizing mAbs in combination with a phage antibody library and a PSIF-based screening system. This method provided one-step screening of cell-internalization of hundreds of "monoclonal" candidates. This is the main advantage of the present system over the old screening system, which required handling a "polyclonal" pool of mAbs.[6,7] The innovative feature of our method is the use of PSIF as a fusion partner for antibodies in scFv format, thus facilitating the identification of antibody fragments capable of efficient internalization. The scFv fusion is much easier than the chemical conjugation of the antibody to a cytotoxic drug. In principle, this method can be applied to other phage libraries, such as nonimmune phage antibody libraries[35,45] or synthetic

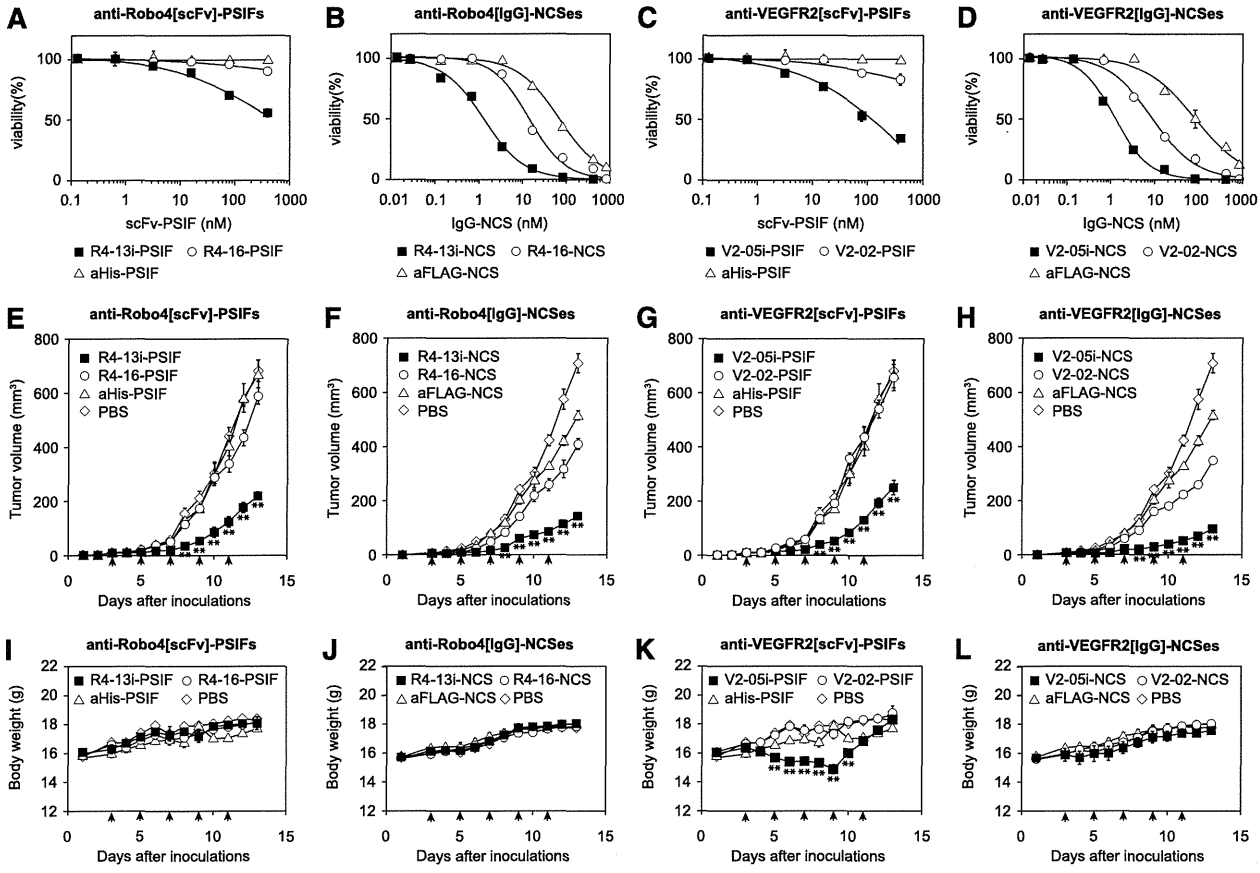

Figure 5. Enhanced anti-tumor effect of cell-internalizing mAbs. (A-D) Cytotoxicity of scFv-PSIF and IgG-NCS against MS1 cells. MS1 cells were incubated with serially diluted mAb-drug conjugates for 24 hours. Cell viability was then measured using a WST-8 assay. Closed square, internalizing mAbs; open circle, low-internalizing mAbs; open triangle, negative controls. (A) anti-Robo4[scFv]-PSIFs, (B) anti-Robo4[IgG]-NCSes, (C) anti-VEGFR2[scFv]-PSIFs, (D) anti-VEGFR2[IgG]-NCSes. Anti-His[scFv]-PSIF and anti-FLAG[IgG]-NCS were used as negative controls. Values are shown as means ± SD. (E-H) Antitumor effects of scFv-PSIFs or IgG-NCSes. B16BL6 cells were inoculated intracutaneously into C57BL6 mice on day 0. On days 3, 5, 7, 9, and 11, mAb-drug conjugates were intravenously administered *(arrow heads)*. Tumor volume was calculated using the following formula: tumor volume (mm^3) = {major axis of tumor (mm)} × {minor axis of tumor (mm)}^{2} × 0.4. Closed square, internalizing mAbs; open circle, low-internalizing mAbs; open triangle, negative controls (anti-His[scFv]-PSIF or anti-FLAG[IgG]-NCS); open diamond, PBS. (E) Anti-Robo4[scFv]-PSIFs, (F) anti-Robo4[IgG]-NCSes, (G) anti-VEGFR2[scFv]-PSIFs, (H) anti-VEGFR2[IgG]-NCSes. Values are shown as means ± SEM. $^{**}P < 0.01$; internalizing mAbs versus low-internalizing mAbs by Bonferroni post hoc analysis with two-way ANOVA (n = 6). (I-L) Change in body weight during therapy experiment. Closed square, internalizing mAbs; open circle, low-internalizing mAbs; open triangle, negative controls (anti-His[scFv]-PSIF or anti-FLAG[IgG]-NCS); open diamond, PBS. (I) anti-Robo4[scFv]-PSIFs, (J) anti-Robo4[IgG]-NCSes, (K) anti-VEGFR2[scFv]-PSIFs, (L) anti-VEGFR2[IgG]-NCSes. Values are shown as means ± SEM. $^{**}P < 0.01$; internalizing mAbs versus PBS by Bonferroni post hoc analysis with two-way ANOVA (n = 6).

human phage antibody libraries,[46,47] which have already been developed. This system can expand the versatility of phage display systems, which will thus contribute to the development of other cell-internalizing antibodies against various types of antigens for effective cancer therapy.

A comparison of cell-internalizing mAbs with low-internalizing mAbs revealed the strength of the cell-internalizing mAbs in terms of the biodistribution and therapeutic effects. Until now, how internalization contributes to the biodistribution of mAbs has been unclear. In this report, we could use a comparative study to clarify this question because we produced both cell-internalizing mAbs and low-internalizing mAbs with similar binding affinities. As a result, more cell-internalizing mAbs than low-internalizing mAbs were significantly accumulated in the tumor. This is the first evidence to support that mAbs with high internalization activity have greater tumor-targeting potency. This information is also useful for other applications that benefit from cell-internalizing mAbs, such as liposomal drugs, bioactive proteins/peptides, and viral vectors.[48,49]

Until now, the usefulness of Robo4-targeted therapy has not been established. Therapy to target VEGF-VEGFR signaling is already common, but the risk of side effects must be addressed.[31-33] Although VEGFR expression is upregulated on tumor vessels, it is also observed on the endothelium in healthy tissues. Previous reports also mentioned the toxicity associated with the anti-VEGFR therapies in mouse models[50] and the clinical trial.[51] Therefore, alternative therapies that target tumor angiogenesis are desired. In the present study, we revealed the possibility that anti-Robo4 ADCs were safer than anti-VEGFR2 ADCs, although they had similar antitumor effects. The findings from immunofluorescence and biodistribution studies also support the notion that anti-Robo4 mAbs could accumulate in the tumor without distributing to normal tissues. This is the first finding of Robo4-targeted therapy and suggests that Robo4 is a potential alternative target for tumor vascular targeting. Of course, additional experiments are needed to establish anti-Robo4 as a novel tool in tumor vascular targeting. For example, the pathological observations of normal blood vessels, in-depth toxicological analysis,

or the efficacy against other clinical relevant tumor models, are important for the successful story. Such basic analyses regarding Robo4 might accelerate the development of novel medicines that target tumor angiogenesis, including anti-Robo4 ADCs.

Acknowledgments

This study was supported by Grant-in-Aid for Scientific research (B) and Grant-in-Aid for Scientific Research on Innovative Areas from the Ministry of Education, Culture, Sports, Science, and Technology of Japan and the Japan Society for the Promotion of Science; Strategic Japanese-Swiss Cooperative Program from Japan Science and Technology Agency (JST) and the Swiss Federal Institute of Technology Zurich.

Authorship

Contribution: Y.M. designed the study; M.Y. and Y. Tsumori performed the experiments; Y.M. and M.Y. analyzed the data; Y.M. and M.Y. wrote the initial manuscript; S.T. and Y. Tsutsumi contributed to the phage display; Y.Y. and N.O. contributed to animal experiments; Y.O., W.C.A., and T.D. contributed to Robo4 related analysis; Y.M. and S.N. were responsible for the overall project. All authors edited the manuscript.

Conflict-of-interest disclosure: The authors declare no competing financial interests.

Correspondence: Yohei Mukai and Shinsaku Nakagawa, Laboratory of Biotechnology and Therapeutics, Graduate School of Pharmaceutical Sciences, Osaka University, 1–6 Yamadaoka, Suita, Osaka 565–0871, Japan; e-mail: y-mukai@nibio.go.jp and nakagawa@phs.osaka-u.ac.jp.

References

1. Alley SC, Okeley NM, Senter PD. Antibody-drug conjugates: targeted drug delivery for cancer. *Curr Opin Chem Biol.* 2010;14(4):529-537.
2. Isakoff SJ, Baselga J. Trastuzumab-DM1: building a chemotherapy-free road in the treatment of human epidermal growth factor receptor 2-positive breast cancer. *J Clin Oncol.* 2011;29(4): 351-354.
3. Ansell SM. Brentuximab vedotin: delivering an antimitotic drug to activated lymphoma cells. *Expert Opin Investig Drugs.* 2011;20(1):99-105.
4. Reichert JM. Antibody-based therapeutics to watch in 2011. *MAbs.* 2011;3(1):76-99.
5. Gerber HP, Senter PD, Grewal IS. Antibody drug-conjugates targeting the tumor vasculature: Current and future developments. *MAbs.* 2009; 1(3):247-253.
6. Poul MA, Becerril B, Nielsen UB, et al. Selection of tumor-specific internalizing human antibodies from phage libraries. *J Mol Biol.* 2000;301(5): 1149-1161.
7. An F, Drummond DC, Wilson S, et al. Targeted drug delivery to mesothelioma cells using functionally selected internalizing human single-chain antibodies. *Mol Cancer Ther.* 2008;7(3): 569-578.
8. Mukai Y, Sugita T, Yamato T, et al. Creation of novel Protein Transduction Domain (PTD) mutants by a phage display-based high-throughput screening system. *Biol Pharm Bull.* 2006;29(8):1570-1574.
9. Chaudhary VK, FitzGerald DJ, Adhya S, et al. Activity of a recombinant fusion protein between transforming growth factor type alpha and Pseudomonas toxin. *Proc Natl Acad Sci USA.* 1987;84(13):4538-4542.
10. Kreitman RJ, Wilson WH, Bergeron K, et al. Efficacy of the anti-CD22 recombinant immunotoxin BL22 in chemotherapy-resistant hairy-cell leukemia. *N Engl J Med.* 2001;345(4): 241-247.
11. Pastan I, FitzGerald D. Pseudomonas exotoxin: chimeric toxins. *J Biol Chem.* 1989;264(26): 15157-15160.
12. Legg JA, Herbert JMJ, Clissold P, et al. Slits and Roundabouts in cancer, tumour angiogenesis and endothelial cell migration. *Angiogenesis.* 2008; 11(1):13-21.
13. Huminiecki L, Bicknell R. In silico cloning of novel endothelial-specific genes. *Genome Res.* 2000; 10(11):1796-1806.
14. Huminiecki L, Gorn M, Suchting S, et al. Magic roundabout is a new member of the roundabout receptor family that is endothelial specific and expressed at sites of active angiogenesis. *Genomics.* 2002;79(4):547-552.
15. Smith-Berdan S, Nguyen A, Hassanein D, et al. Robo4 cooperates with CXCR4 to specify hematopoietic stem cell localization to bone marrow niches. *Cell Stem Cell.* 2011;8(1):72-83.
16. Park KW, Morrison CM, Sorensen LK, et al. Robo4 is a vascular-specific receptor that inhibits endothelial migration. *Dev Biol.* 2003;261(1): 251-267.
17. Seth P, Lin Y, Hanai J, et al. Magic roundabout, a tumor endothelial marker: expression and signaling. *Biochem Biophys Res Commun.* 2005; 332(2):533-541.
18. Okada Y, Yano K, Jin E, et al. A three-kilobase fragment of the human Robo4 promoter directs cell type-specific expression in endothelium. *Circ Res.* 2007;100(12):1712-1722.
19. Okada Y, Jin E, Nikolova-Krstevski V, et al. A GABP-binding element in the Robo4 promoter is necessary for endothelial expression in vivo. *Blood.* 2008;112(6):2336-2339.
20. Jones CA, London NR, Chen H, et al. Robo4 stabilizes the vascular network by inhibiting pathologic angiogenesis and endothelial hyperpermeability. *Nat Med.* 2008;14(4):448-453.
21. Jones CA, Nishiya N, London NR, et al. Slit2-Robo4 signalling promotes vascular stability by blocking Arf6 activity. *Nat Cell Biol.* 2009; 11(11):1325-1331.
22. Marlow R, Binnewies M, Sorensen LK, et al. Vascular Robo4 restricts proangiogenic VEGF signaling in breast. *Proc Natl Acad Sci USA.* 2010;107(23):10520-10525.
23. Koch AW, Mathivet T, Larrivée B, et al. Robo4 maintains vessel integrity and inhibits angiogenesis by interacting with UNC5B. *Dev Cell.* 2011;20(1):33-46.
24. Kerbel RS. Tumor angiogenesis. *N Engl J Med.* 2008;358(19):2039-2049.
25. Paleolog EM. Angiogenesis in rheumatoid arthritis. *Arthritis Res.* 2002;4(Suppl 3):S81-S90.
26. Tonnesen MG, Feng X, Clark RA. Angiogenesis in wound healing. *J Investig Dermatol Symp Proc.* 2000;5(1):40-46.
27. Olsson AK, Dimberg A, Kreuger J, et al. VEGF receptor signalling - in control of vascular function. *Nat Rev Mol Cell Biol.* 2006;7(5):359-371.
28. Crawford Y, Ferrara N. VEGF inhibition: insights from preclinical and clinical studies. *Cell Tissue Res.* 2009;335(1):261-269.
29. Wicki A, Rochlitz C, Orleth A, et al. Targeting tumor-associated endothelial cells: anti-VEGFR2 immunoliposomes mediate tumor vessel disruption and inhibit tumor growth. *Clin Cancer Res.* 2012;18(2):454-464.
30. Witmer AN, Dai J, Weich HA, et al. Expression of vascular endothelial growth factor receptors 1, 2, and 3 in quiescent endothelia. *J Histochem Cytochem.* 2002;50(6):767-777.
31. Kamba T, McDonald DM. Mechanisms of adverse effects of anti-VEGF therapy for cancer. *Br J Cancer.* 2007;96(12):1788-1795.
32. Eremina V, Jefferson JA, Kowalewska J, et al. VEGF inhibition and renal thrombotic microangiopathy. *N Engl J Med.* 2008;358(11):1129-1136.
33. Choueiri TK, Mayer EL, Je Y, et al. Congestive heart failure risk in patients with breast cancer treated with bevacizumab. *J Clin Oncol.* 2011; 29(6):632-638.
34. Yoshikawa M, Mukai Y, Okada Y, et al. Ligand-independent assembly of purified soluble magic roundabout (Robo4), a tumor-specific endothelial marker. *Protein Expr Purif.* 2008;61(1):78-82.
35. Imai S, Mukai Y, Nagano K, et al. Quality enhancement of the non-immune phage scFv library to isolate effective antibodies. *Biol Pharm Bull.* 2006;29(7):1325-1330.
36. Yoshikawa M, Mukai Y, Tsunoda S, et al. Modifying the antigen-immunization schedule improves the variety of monoclonal antibodies obtained from immune-phage antibody libraries against HIV-1 Nef and Vif. *J Biosci Bioeng.* 2011; 111(5):597-599.
37. Yamamoto Y, Tsutsumi Y, Yoshioka Y, et al. Site-specific PEGylation of a lysine-deficient TNF-alpha with full bioactivity. *Nat Biotechnol.* 2003;21(5):546-552.
38. Hunter WM, Greenwood FC. Preparation of iodine-131 labelled human growth hormone of high specific activity. *Nature.* 1962;194:495-496.
39. Mellman I. Endocytosis and molecular sorting. *Annu Rev Cell Dev Biol.* 1996;12:575-625.
40. Holliger P, Hudson PJ. Engineered antibody fragments and the rise of single domains. *Nat Biotechnol.* 2005;23(9):1126-1136.
41. Pavlinkova G, Beresford GW, Booth BJ, et al. Pharmacokinetics and biodistribution of engineered single-chain antibody constructs of MAb CC49 in colon carcinoma xenografts. *J Nucl Med.* 1999;40(9):1536-1546.
42. Schneider DW, Heitner T, Alicke B, et al. In vivo biodistribution, PET imaging, and tumor accumulation of 86Y- and 111In-antimindir/RG-1,

engineered antibody fragments in LNCaP tumor-bearing nude mice. *J Nucl Med.* 2009; 50(3):435-443.

43. Maeda H. SMANCS and polymer-conjugated macromolecular drugs: advantages in cancer chemotherapy. *Adv Drug Deliv Rev.* 2001;46(1-3): 169-185.
44. Kappen LS, Goldberg IH. Activation and inactivation of neocarzinostatin-induced cleavage of DNA. *Nucleic Acids Res.* 1978; 5(8):2959-2967.
45. Okamoto T, Mukai Y, Yoshioka Y, et al. Optimal construction of non-immune scFv phage display libraries from mouse bone marrow and spleen established to select specific scFvs efficiently binding to antigen. *Biochem Biophys Res Commun.* 2004;323(2): 583-591.
46. Silacci M, Brack S, Schirru G, et al. Design, construction, and characterization of a large synthetic human antibody phage display library. *Proteomics.* 2005;5(9): 2340-2350.
47. Villa A, Lovato V, Bujak E, et al. A novel synthetic naïve human antibody library allows the isolation of antibodies against a new epitope of oncofetal fibronectin. *MAbs.* 2011; 3(3):264-272.
48. Sapra P, Allen TM. Internalizing antibodies are necessary for improved therapeutic efficacy of antibody-targeted liposomal drugs. *Cancer Res.* 2002;62(24):7190-7194.
49. Pastan I, Hassan R, Fitzgerald DJ, et al. Immunotoxin therapy of cancer. *Nat Rev Cancer.* 2006;6(7):559-565.
50. Chinnasamy D, Yu Z, Theoret MR, et al. Gene therapy using genetically modified lymphocytes targeting VEGFR-2 inhibits the growth of vascularized syngenic tumors in mice. *J Clin Invest.* 2010;120(11):3953-3968.
51. Nagayama H, Matsumoto K, Isoo N, et al. Gastrointestinal bleeding during anti-angiogenic peptide vaccination in combination with gemcitabine for advanced pancreatic cancer. *Clin J Gastroenterol.* 2010;3(6):307-317.

A Baculoviral Display System to Assay Viral Entry

Manami Iida,[a,#] Takeshi Yoshida,[a,#] Akihiro Watari,[a] Kiyohito Yagi,[a] Takao Hamakubo,[b] and Masuo Kondoh*[,a]

[a] *Laboratory of Bio-Functional Molecular Chemistry, Graduate School of Pharmaceutical Sciences, Osaka University; Suita, Osaka 565–0871, Japan: and* [b] *Department of Quantitative Biology and Medicine, Research Center for Advanced Science and Technology, The University of Tokyo; Tokyo 153–8904, Japan.*
Received August 9, 2013; accepted August 22, 2013

In this study, we evaluated a baculoviral display system for analysis of viral entry by using a recombinant adenovirus (Ad) carrying a luciferase gene and budded baculovirus (BV) that displays the adenoviral receptor, coxsackievirus and adenovirus receptor (CAR). CAR-expressing B16 cells (B16-CAR cells) were infected with luciferase-expressing Ad vector in the presence of BV that expressed or lacked CAR (CAR-BV and mock-BV, respectively). Treatment with mock-BV even at doses as high as 5 μg/mL failed to attenuate the luciferase activity of B16-CAR cells. In contrast, treatment with CAR-BV with doses as low as 0.5 μg/mL significantly decreased the luciferase activity of infected cells, which reached 65% reduction at 5 μg/mL. These findings suggest that a receptor-displaying BV system could be used to evaluate viral infection.

Key words baculovirus; virus; infection; receptor

The process of viral infection involves entry of the virus into the cell, followed by replication of the viral genome and other viral components in the host cell.[1] Whereas the molecular mechanisms underlying viral replication have largely been elucidated, the key molecules for entry, the viral receptors on host cells, have never been fully identified. Most host receptors are integral membrane proteins, and it is difficult to prepare their recombinant proteins because of their hydrophobicity. Since recombinant proteins are needed to screen inhibitors for viral entry and to produce antibodies against host receptors, preparation of inhibitors, such as chemicals, peptides and antibodies, for viral entry has been delayed.

The baculoviral expression system in insect cells has been widely used for preparation of recombinant proteins.[2] Hamakubo and colleagues found that baculoviral particles are released from baculovirus-infected cells; the membranes of these budded baculovirus (BV) display host-cell-derived membrane proteins.[3] Interestingly, the activity and topology of these host-origin proteins remain intact in the baculoviral membrane.[4] Moreover, a baculoviral envelope protein gp64 trasngenic mice were generated, and method to generate monoclonal antibodies against membrane proteins by immunization of gp64 transgenic mice with membrane protein-displayed baculovirus has been established.[5] These findings suggest that a baculoviral display system may be useful for assaying viral entry, leading to creation of monoclonal antibodies against host receptors.

In the present study, we investigated whether a baculoviral display system work as an assay system for viral entry using recombinant adenovirus (Ad) vector and a receptor for Ad, coxsackievirus and adenovirus receptor (CAR).[6]

MATERIALS AND METHODS

Cell Culture Mouse melanoma B16-CAR cells[7] were cultured in Dulbecco's modified Eagle's medium (DMEM) supplemented with 10% fetal calf serum (FCS) and 2 mg/mL G418. 293 cells were cultured in DMEM supplemented with 10% FCS. Sf9 cells (Invitrogen, Gaithersburg, MD, U.S.A.) were cultured in Grace's insect cell culture medium supplemented with 10% FCS.

Preparation of Recombinant Ad Vector An improved *in vitro* ligation method[8] was used to generate a recombinant type 5 Ad vector that encoded a fusion protein comprising enhanced green fluorescence protein and firefly luciferase (EGFPLuc). The recombinant Ad vector (Ad-EGFPLuc) was purified from transfected cells by using $CsCl_2$ gradient centrifugation. Viral titers were determined spectrophotometrically.[9]

Preparation of Recombinant Baculoviruses Recombinant BVs were prepared by using the Bac-to-Bac Baculovirus Expression System (Invitrogen) according to the manufacturer's protocol. Sf9 cells were transduced with the CAR-encoding bacmid, recombinant CAR-BV were recovered by centrifugation of the conditioned medium,[10] and Sf9 cells were infected with recombinant CAR-BV. At 72 h after infection, the culture supernatant of the infected Sf9 cells was centrifuged to pellet recombinant CAR-BV, which were resuspended in Tris-buffered saline and stored at 4°C until use.

Western Blotting Mock-BV, CAR-BV, and B16-CAR cells were lysed in lysis buffer (25 mM Tris–HCl [pH 7.5], 1% Triton X-100, 0.5% sodium deoxycholate, 150 mM NaCl, 5 mM ethylenediaminetetraacetic acid (EDTA)) containing protease inhibitors (Sigma, St. Louis, MO, U.S.A.). The protein content of the resulting lysates was measured by using the BCA protein assay kit (Pierce Chemical, Rockford, IL, U.S.A.), with bovine serum albumin as the standard. Samples of cellular lysates (20 μg) and BV lysates (5 μg) underwent sodium dodecyl sulfate–polyacrylamide gel electrophoresis followed by blotting of proteins to a polyvinylidene difluoride membrane. The membrane was treated with 5% skim milk to inhibit nonspecific binding, incubated with an anti-goat CAR antibody (R&D Systems, Minneapolis, MN, U.S.A.), and then incubated with a peroxidase-labeled secondary antibody. Immunoreactive bands were visualized by using chemiluminescence reagents (GE Healthcare, Buckinghamshire, U.K.).

Infection Assay Aliquots of Ad-EGFPLuc vector (4×10^7

The authors declare no conflict of interest.

[#] These authors contributed equally to this work.

* To whom correspondence should be addressed. e-mail: masuo@phs.osaka-u.ac.jp

viral particles per mL) were incubated with mock-BV or CAR-BV (0.5 or 5 μg/mL) and an anti-BV gp64 antibody (0.065 or 0.65 μg/mL; AcV1, Santa Cruz Biotechnology, CA, U.S.A.) for 2 h at 37°C to prevent non-specific binding of gp64 to cells. B16-CAR cells were seeded onto 96-well plates (2×10^4 cells per well); 50 μL of the mixture of Ad vector and BVs was added to each well and incubated for 15 min, after which the medium was replaced with fresh growth medium. After an additional 24 h of culture, the luciferase activity in the lysates was measured by using a luminometer.

Statistical Analysis The data were analyzed for statistical significance by Student's *t*-test.

RESULTS AND DISCUSSION

First, we prepared CAR-displaying BV. Lysates of CAR-B16 cells, a mouse myeloma line that expresses mouse CAR, yielded two bands, at 40 and 46 kDa (Fig. 1). In contrast, lysates of CAR-BV showed not only the 40-kDa form but also several bands lower and upper than 40 kDa (Fig. 1); these bands likely represent post-translational modifications. CAR contains two *N*-glycosylation sites and two disulfide-bonded loops in the extracellular domain. The putative molecular sizes of CAR are 40 and 46 kDa, in its non-glycosylated form and glycosylated forms, respectively.[6] Protein folding and post-translational processing, particularly *N*-glycosylation, in insect cells differs markedly from that in mammal cells.[11–13] For example, prolactin receptor expressed in insect cells was 29 kDa larger than that expressed in mammalian cells; this difference was attributed to *N*-glycosylation and ubiquitination.[14]

To investigate whether CAR-BV inhibited adenoviral entry, B16-CAR cells were infected with Ad vector expressing luciferase in the presence of mock-BV or CAR-BV. Whereas treatment with mock-BV at doses as high as 5 μg/mL did not attenuate the luciferase activity of the infected B16-CAR cells, treatment with as little as 0.5 μg/mL CAR-BV significantly decreased their luciferase activity, which reaching 65% reduction at 5 μg/mL (Fig. 2). These findings indicate that CAR-BV prevented the infection of cells by Ad vector. In support of our finding, recombinant prolactin receptor expressed in insect cells and prolactin receptor purified from rabbit mammary gland showed similar specificity and affinity to prolactin.[14] Accordingly, the post-translational modification of CAR in insect cells may not hamper the ability of Ad vector to bind to its receptor.

Our current findings suggest that a baculoviral display system may be useful in the analysis of viral infection, which involves binding of the viral envelope to the viral receptor in the membrane of the host cell. Baculoviral display systems have also been used widely to generate monoclonal antibodies against the extracellular regions of membrane proteins.[3,15] Future applications of baculoviral display systems might contribute the analysis of the mechanisms underlying the entry of pathogens into host cells and the generation of inhibitors of viral entry.

Acknowledgments We thank Prof. H. Mizuguchi (Osaka University) and the members of our laboratory for providing us CAR cDNA and CAR-expressing B16 cells, and useful comments, respectively. This work was supported by a Grant-in-Aid for Scientific Research from the Ministry of Education, Culture, Sports, Science and Technology of Japan (24390042), by a Health and Labour Sciences Research Grant from the Ministry of Health, Labor, and Welfare of Japan, the Takeda Science Foundation and the Nakatomi Foundation.

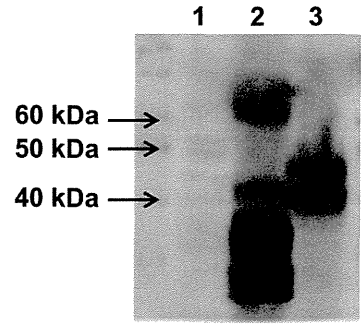

Fig. 1. Preparation of CAR-Displaying BV

Lysates of mock-BV (5 μg, lane 1), CAR-BV (5 μg, lane 2), and CAR-B16 cells (20 μg, lane 3) underwent Western blotting by using a polyclonal goat anti-CAR antibody and a peroxidase-labeled secondary antibody. The arrows indicate the positions of marker proteins.

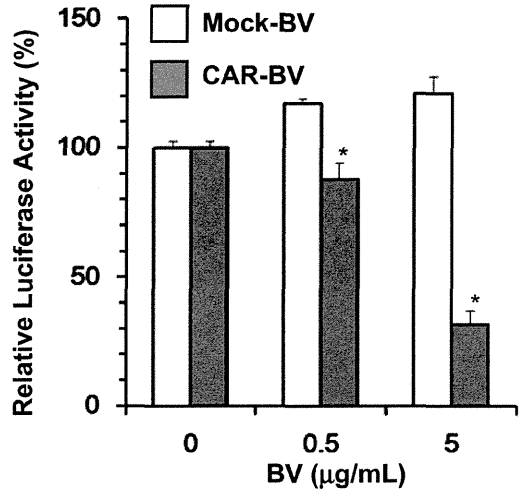

Fig. 2. Effects of CAR-Displaying BV on Ad Vector Infection

Ad vectors (4×10^7 viral particles per mL) were incubated with mock-BV or CAR-BV at 0, 0.5, or 5 μg/mL for 2 h at 37°C. B16-CAR cells were exposed to the Ad–BV mixtures, cultured for 24 h in fresh medium, lysed, and evaluated for luciferase activity. Data are given as luciferase activity relative to that of cells not exposed to BV. Data are shown as mean±S.D. (n=3). *Significant difference compared with mock-BV ($p<0.05$).

REFERENCES

1) Cosset FL, Lavillette D. Cell entry of enveloped viruses. *Adv. Genet.*, **73**, 121–183 (2011).
2) Bieniossek C, Imasaki T, Takagi Y, Berger I. MultiBac: expanding the research toolbox for multiprotein complexes. *Trends Biochem. Sci.*, **37**, 49–57 (2012).
3) Tanaka T, Takeno T, Watanabe Y, Uchiyama Y, Murakami T, Yamashita H, Suzuki A, Aoi R, Iwanari H, Jiang SY, Naito M, Tachibana K, Doi T, Shulman AI, Mangelsdorf DJ, Reiter R, Auwerx J, Hamakubo T, Kodama T. The generation of monoclonal antibodies against human peroxisome proliferator-activated receptors (PPARs). *J. Atheroscler. Thromb.*, **9**, 233–242 (2002).
4) Sakihama T, Masuda K, Sato T, Doi T, Kodama T, Hamakubo T. Functional reconstitution of G-protein-coupled receptor-mediated adenylyl cyclase activation by a baculoviral co-display system. *J.*

Biotechnol., **135**, 28–33 (2008).
5) Saitoh R, Ohtomo T, Yamada Y, Kodama N, Nezu J, Kimura N, Funahashi S, Furugaki K, Yoshino T, Kawase Y, Kato A, Ueda O, Jishage K, Suzuki M, Fukuda R, Arai M, Iwanari H, Takahashi K, Sakihama T, Ohizumi I, Kodama T, Tsuchiya M, Hamakubo T. Viral envelope protein gp64 transgenic mouse facilitates the generation of monoclonal antibodies against exogenous membrane proteins displayed on baculovirus. *J. Immunol. Methods*, **322**, 104–117 (2007).
6) Arnberg N. Adenovirus receptors: implications for targeting of viral vectors. *Trends Pharmacol. Sci.*, **33**, 442–448 (2012).
7) Yamashita M, Ino A, Kawabata K, Sakurai F, Mizuguchi H. Expression of coxsackie and adenovirus receptor reduces the lung metastatic potential of murine tumor cells. *Int. J. Cancer*, **121**, 1690–1696 (2007).
8) Mizuguchi H, Kay MA. A simple method for constructing E1- and E1/E4-deleted recombinant adenoviral vectors. *Hum. Gene Ther.*, **10**, 2013–2017 (1999).
9) Maizel JV Jr, White DO, Scharff MD. The polypeptides of adenovirus. I. Evidence for multiple protein components in the virion and a comparison of types 2, 7A, and 12. *Virology*, **36**, 115–125 (1968).
10) Saeki R, Kondoh M, Kakutani H, Tsunoda S, Mochizuki Y, Hamakubo T, Tsutsumi Y, Horiguchi Y, Yagi K. A novel tumor-targeted therapy using a claudin-4-targeting molecule. *Mol. Pharmacol.*, **76**, 918–926 (2009).
11) Altmann F, Staudacher E, Wilson IB, Marz L. Insect cells as hosts for the expression of recombinant glycoproteins. *Glycoconj. J.*, **16**, 109–123 (1999).
12) Voss T, Ergulen E, Ahorn H, Kubelka V, Sugiyama K, Maurer-Fogy I, Glossl J. Expression of human interferon omega 1 in Sf9 cells. No evidence for complex-type *N*-linked glycosylation or sialylation. *Eur. J. Biochem.*, **217**, 913–919 (1993).
13) Yeh JC, Seals JR, Murphy CI, van Halbeek H, Cummings RD. Site-specific *N*-glycosylation and oligosaccharide structures of recombinant HIV-1 gp120 derived from a baculovirus expression system. *Biochemistry*, **32**, 11087–11099 (1993).
14) Cahoreau C, Petridou B, Cerutti M, Djiane J, Devauchelle G. Expression of the full-length rabbit prolactin receptor and its specific domains in baculovirus infected insect cells. *Biochimie*, **74**, 1053–1065 (1992).
15) Hayashi I, Takatori S, Urano Y, Miyake Y, Takagi J, Sakata-Yanagimoto M, Iwanari H, Osawa S, Morohashi Y, Li T, Wong PC, Chiba S, Kodama T, Hamakubo T, Tomita T, Iwatsubo T. Neutralization of the gamma-secretase activity by monoclonal antibody against extracellular domain of nicastrin. *Oncogene*, **31**, 787–798 (2012).

Cancer Medicine

Open Access

SHORT REPORT

Expression of Eph receptor A10 is correlated with lymph node metastasis and stage progression in breast cancer patients

Kazuya Nagano[1], So-ichiro Kanasaki[1,2], Takuya Yamashita[1,2], Yuka Maeda[1,2], Masaki Inoue[1], Kazuma Higashisaka[1,2], Yasuo Yoshioka[1,2,3], Yasuhiro Abe[1], Yohei Mukai[1], Haruhiko Kamada[1,3], Yasuo Tsutsumi[1,2,3] & Shin-ichi Tsunoda[1,2,3]

[1]Laboratory of Biopharmaceutical Research, National Institute of Biomedical Innovation, 7-6-8 Saito-Asagi, Ibaraki, Osaka 567-0085, Japan
[2]Graduate School of Pharmaceutical Sciences, Osaka University, 1-6 Yamadaoka, Suita, Osaka 565-0871, Japan
[3]The Center for Advanced Medical Engineering and informatics, Osaka University, 1-6 Yamadaoka, Suita, Osaka 565-0871, Japan

Keywords
Breast cancer, Eph receptor A10, lymph node metastasis

Correspondence
Shin-ichi Tsunoda, Laboratory of Biopharmaceutical Research, National Institute of Biomedical Innovation, 7-6-8 Saito-Asagi, Ibaraki, Osaka 567-0085, Japan.
Tel: +81-72-641-9814; Fax: +81-72-641-9817;
E-mail: tsunoda@nibio.go.jp

Funding Information
This study was supported in part by Grants-in-Aid for Scientific Research and Project for Development of Innovative Research on Cancer Therapeutics from the Ministry of Education, Culture, Sports, Science and Technology of Japan. This study was also supported in part by Health Labor Sciences Research Grants from the Ministry of Health, Labor and Welfare of Japan.

Received: 30 July 2013; Revised: 30 September 2013; Accepted: 4 October 2013

***Cancer Medicine* 2013; 2(6): 972–977**

doi: 10.1002/cam4.156

Abstract

Eph receptor A10 (EphA10) is a valuable breast cancer marker that is highly expressed in breast cancer tissues by comparison with normal breast tissues, as we previously reported. However, the role of EphA10 expression in breast cancer is not well understood. Here, we have analyzed the expression of EphA10 at the mRNA- and protein-level in clinical breast cancer tissues and then evaluated the relationship with clinicopathological parameters for each sample. EphA10 mRNA expression was quantified by real-time polymerase chain reaction using complimentary DNA (cDNA) samples derived from breast cancer patients. Lymph node (LN) metastasis and stage progression were significantly correlated with EphA10 expression at the mRNA level ($P = 0.0091$ and $P = 0.034$, respectively). Furthermore, immunohistochemistry (IHC) staining of breast cancer tissue microarrays (TMAs) revealed that EphA10 expression at the protein level was also associated with LN metastasis and stage progression ($P = 0.016$ and $P = 0.011$, respectively). These results indicate that EphA10 expression might play a role in tumor progression and metastasis. Our findings will help elucidate the role of EphA10 in clinical breast cancer progression.

Introduction

Eph receptors comprise the largest subgroup of the receptor tyrosine kinase family of proteins. Currently, nine type-A (EphA1–A8, EphA10) and five type-B (EphB1–B4, EphB6) molecules are known in mammals. Eph family receptors play important roles in physiological development such as neural development [1] and glucose homeostasis [2]. In addition, several Eph family receptors were implicated in various aspects of the tumor malignancy, including tumorigenesis [3, 4], proliferation [5, 6], vasculogenesis [7, 8] or metastasis [9–11]. Indeed, EphA2 is highly expressed in several kinds of tumor, and this enhanced expression is thought to

be related to tumor progression [3, 5, 9, 10]. Currently, clinical trials of a EphA2-targeting drug are ongoing [12]. Therefore, the expression profiles, function, and targeting therapy for Eph family receptors are directly related to cancer biology and drug development.

EphA10 is a novel breast cancer marker that was originally discovered by ourselves using a proteomics approach [13]. Prior to this discovery, EphA10 was only known to be expressed in the testis at the mRNA level [14]. Our group has developed an "antibody proteomics system", which facilitates the validation of biomarker candidates identified from proteome analyses [13]. Using this method, we previously revealed that EphA10 is expressed in many breast cancer tissues compared to normal tissues [13]. However, the function of EphA10 has not been fully analyzed. Consequently, the relationship between EphA10 and clinical tumor progression is poorly understood.

Here, we first analyzed the statistical relationship between EphA10 mRNA expression in clinical tumor tissues and their clinicopathological parameters. Next, we evaluated the correlation with EphA10 expression at the protein level, which is important to fulfill the EphA10 function. This data will help elucidate the role of EphA10 in clinical breast cancer progression.

Material and Methods

Analysis of EphA10 mRNA expression by real-time polymerase chain reaction

Complimentary DNAs (cDNA) derived from human breast tumors were purchased from OriGene Technologies (Rockville, MD). The 20 μL polymerase chain reaction (PCR) mixture included 1 μL of cDNA template, 10 μL of TaqMan Gene Expression Master Mix, and 1 μL of TaqMan probe (EphA10:Hs01017018_m1 or actin-beta:Hs99999903_m1) (Life Technologies, Carlsbad, CA). Reactions were performed according to the manufacturer's instructions. The threshold cycles were determined using the default settings. EphA10 mRNA expression levels were normalized against actin-beta. Cases with greater or less than the median value were classified into a high or low expression group, respectively (Table 1). In Figure 1, we display the EphA10 mRNA expression level as the ratio against the median.

Analysis of EphA10 protein expression by immunohistochemistry staining

Breast cancer tissue microarrays (TMAs) (US Biomax, Rockville, MD) were deparaffinated in xylene and rehydrated in ethanol. Epitope retrieval was performed by maintaining the Target Retrieval Solution (Dako, Glostup, Denmark) according to the manufacturer's instructions. After treatment, endogenous peroxidase was blocked with 0.3% H_2O_2 for 5 min. The slides were then incubated with anti-human EphA10 polyclonal antibody (Abgent, San Diego, CA) for 30 min. After washing three times, the slides were incubated for 30 min with Envision+Dual Link (Dako, Glostup, Denmark). Finally, the slides were washed three times and treated in 3,3′-diaminobenzidine and counterstained with hematoxylin. For statistical analysis, study samples were divided into high and low expression groups based on the following two criteria. In terms of distribution, the percentage of positive cells in all tumor cells was scored as 0 (0%), 1 (1–50%), and 2 (51–100%). In terms of quantity, the signal intensity was scored as 0 (no signal), 1 (weak), 2 (moderate), or 3

Table 1. Correlation between EphA10 mRNA expression and clinicopathological characteristics.

		EphA10 mRNA expression		*P* value	
Characteristics	*n*	High *n* (%)	Low *n* (%)	χ^2	Mann–Whitney
Age					
<45	5	2 (40.0)	3 (60.0)	1.00	–
≧45	30	15 (50.0)	15 (50.0)		
Gender					
Male	0	0 (0.0)	0 (0.0)	–	–
Female	35	17 (48.6)	18 (51.4)		
Histological classification					
Invasive ductal carcinoma	32	15 (46.9)	17 (53.1)	0.21	–
Invasive lobular carcinoma	2	2 (100.0)	0 (0.0)		
Squamous cell carcinoma	1	0 (0.0)	1 (100.0)		
pT					
T1	13	6 (46.2)	7 (53.8)	0.23	0.25
T2	18	8 (44.4)	10 (55.6)		
T3	3	3 (100.0)	0 (0.0)		
T4	1	1 (100.0)	0 (0.0)		
pN					
N0	17	5 (29.4)	12 (70.6)	0.045	0.0091
N1	9	6 (66.7)	3 (33.3)		
N2	5	3 (60.0)	2 (40.0)		
N3	4	4 (100.0)	0 (0.0)		
pStage					
I	10	4 (40.0)	6 (60.0)	0.022	0.034
II	13	4 (30.8)	9 (69.2)		
III	12	10 (83.3)	2 (16.7)		

Indication of each pathological parameter is as follows: pT, degree of size of the primary tumor; pN, degree of spread to regional lymph nodes; pStage, degree of cancer progression.

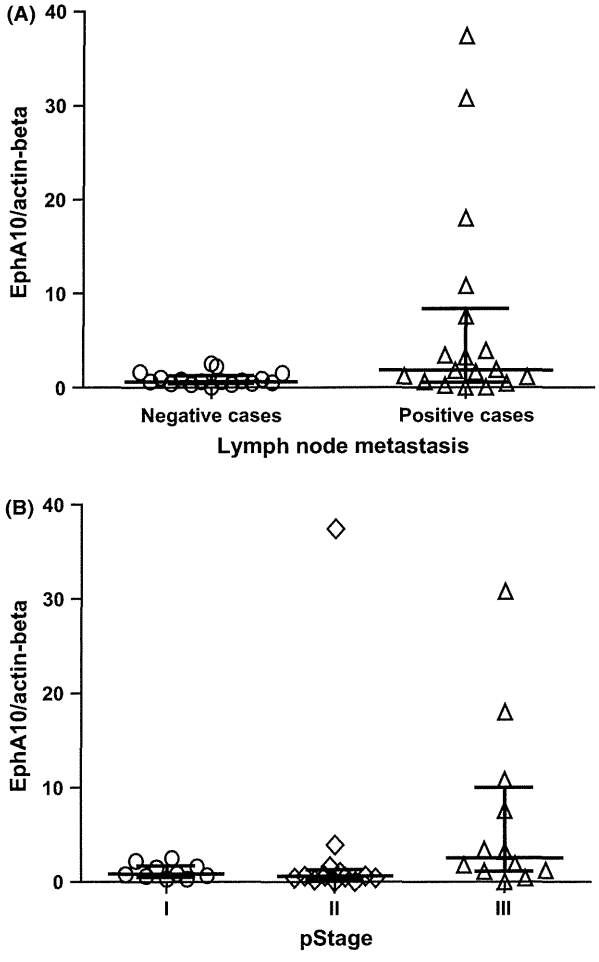

Figure 1. EphA10 mRNA expression level analysis in lymph node (LN)-positive and -negative cases, or stage I, II, and III. EphA10 mRNA expression level in each case was normalized to that of actin-beta. The ratio of EphA10 mRNA expression level against median value was plotted for LN-positive and -negative cases (A), or stage I, II, and III, respectively (B). Differences were evaluated using the Mann–Whitney test ($P = 0.025$) (A) and Kruskal–Wallis test ($P = 0.044$) (B). Bar and range show the median with interquartile range in each group.

(marked). Cases with a total score of ≥3 were classified into the high expression group.

Statistical methods

All analyses were performed using GraphPad Prism 5 version (GraphPad Software Inc., La Jolla, CA). Chi-square or Fisher's exact test were used to compare the categorical variables. Differences between two or three groups were analyzed by the Mann–Whitney or Kruskal–Wallis test, respectively. All hypothesis testing was two-tailed with a significant level of 0.05.

Table 2. Correlation between EphA10 protein expression and clinicopathological characteristics.

		EphA10 protein expression		*P* value	
Characteristics	*n*	High *n* (%)	Low *n* (%)	χ^2	Mann–Whitney
Age					
<45	103	61 (59.2)	42 (40.8)	0.19	–
≧45	199	133 (66.8)	66 (33.2)		
Gender					
Male	2	2 (100.0)	0 (0.0)	0.54	–
Female	300	192 (64.0)	108 (36.0)		
Histological classification					
Invasive ductal carcinoma	272	177 (65.1)	95 (34.9)	0.59	–
Invasive lobular carcinoma	10	5 (50.0)	5 (50.0)		
Invasive papillary carcinoma	6	5 (83.3)	1 (16.7)		
Mucinous carcinoma	2	1 (50.0)	1 (50.0)		
Medullary carcinoma	2	2 (100.0)	0 (0.0)		
Carcinosarcoma	1	1 (100.0)	0 (0.0)		
pT					
T1	21	15 (71.4)	6 (28.6)	0.35	0.96
T2	200	127 (63.5)	73 (36.5)		
T3	46	26 (56.5)	20 (43.5)		
T4	35	26 (74.3)	9 (25.7)		
pN					
N0	154	90 (58.4)	64 (41.6)	0.044	0.016
N1	116	80 (69.0)	36 (31.0)		
N2	26	22 (84.6)	4 (15.4)		
N3	6	3 (50.0)	3 (50.0)		
pStage					
I	9	4 (44.4)	5 (55.6)	0.037	0.011
II	232	143 (61.6)	89 (38.4)		
III	61	47 (77.0)	14 (23.0)		

Indication of each pathological parameter is as follows: pT, degree of size of the primary tumor; pN, degree of spread to regional lymph nodes; pStage, degree of cancer progression.

Results and Discussion

In order to analyze the contribution of EphA10 to clinical breast cancer progression, we evaluated a possible correlation between EphA10 mRNA expression in the clinical tumor tissues and clinicopathological parameters such as primary tumor size (pT), lymph node (LN) metastasis (pN) and stage grouping as indicators of cancer progression (Table 1). Statistical analysis showed that EphA10 expression was independent of age, histological classification, and pT indexes. Nonetheless, EphA10 mRNA expression was positively associated with the progression

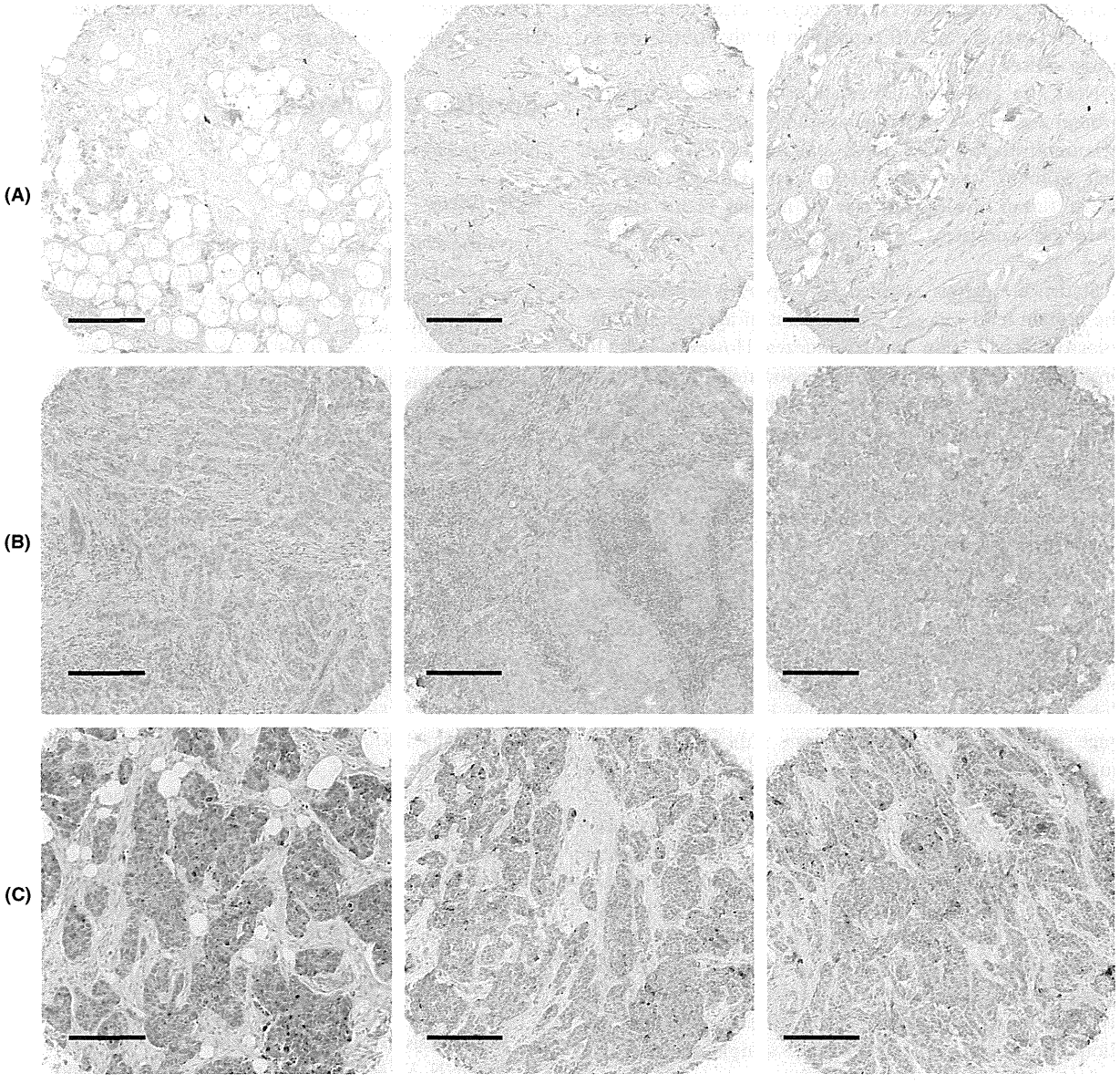

Figure 2. Immunohistochemical staining images in tissue microarray (TMA) with breast tumor and normal tissues. TMAs with breast tumor and normal tissues were stained using anti-EphA10 antibody. Representative images of normal breast tissue (A), EphA10 negative breast cancer tissue (B), and EphA10 positive breast cancer tissues (C) are shown. Scale bar: 200 μm.

of the stage, which strongly supports our previous TMA-based analysis [13]. Furthermore, we found that EphA10 expression was also positively correlated with LN metastasis. Given that a combination of pT and pN values in each case defines stage I–III, these data suggest a significant correlation with LN metastasis might contribute to that with stage progression.

For detailed evaluation of the contribution of EphA10 expression to LN metastasis, we divided all the cases into LN metastasis positive and negative, and then plotted the EphA10 expression levels for the two groups. Figure 1A indicates that patients with elevated levels of EphA10 expression in tumor tissues were positive for LN metastasis. Indeed, a significant difference between LN-positive and -negative cases was observed. Moreover, we similarly analyzed for pStage. Figure 1B indicated that, with the exception of one outlier observed in stage II, EphA10 expression also displayed a significant positive correlation